

Dysregulation of GTPase-activating protein-binding protein1 in the pathogenesis of metabolic dysfunction-associated steatotic liver disease

Received: 16 April 2025

Accepted: 7 August 2025

Published online: 14 August 2025



Qinqin Ouyang^{1,7}, Jiaqi Su^{2,7}, Yixuan Li^{1,7}, Haiping Liao¹, Haiying Guo¹, Yanan Sun¹, Xiaoyu Wang¹, Juan Chen¹, Josephine Thinwa³, Wen-Xing Ding⁴, Herbert Tilg⁵, Fazheng Ren¹✉, Hao Zhang^{1,6}✉ & Rong Liu¹✉

Metabolic dysfunction-associated steatotic liver disease (MASLD) and metabolic dysfunction-associated steatohepatitis (MASH) are two common liver disorders characterized by abnormal lipid accumulation. Our study found reduced levels of GTPase-activating protein-binding protein1 (G3BP1) in patients with MASLD and MASH, suggesting its involvement in these liver disorders. Hepatocyte-specific G3BP1 knockout (G3BP1 HKO) male mice had more severe MASLD and MASH than their corresponding controls. Intriguingly, the G3BP1 HKO MASLD model male mice exhibit dysregulated autophagy, and biochemical analyses demonstrated that G3BP1 promotes autophagosome-lysosome fusion through direct interactions with the SNARE proteins STX17 and VAMP8. We also show that hepatic knockout of G3BP1 promotes de novo lipogenesis, and ultimately found that G3BP1 is required for the nuclear translocation of the well-known liver-lipid-regulating transcription factor TFE3. Taken together, our results suggest that G3BP1 should be investigated as a potential target for developing medical interventions to treat MASLD and MASH.

Metabolic dysfunction-associated steatotic liver disease (MASLD) is a condition characterized by the accumulation of excess fat in the liver of individuals who consume little or no alcohol¹. MASLD is a widespread medical and public health concern^{2–4}. MASLD can progress to metabolic dysfunction-associated steatohepatitis (MASH) as hepatocyte injury and inflammation set in ref. 5, and MASH can further progress to cirrhosis⁶ and hepatocellular carcinoma⁷. Given that these liver lipid disorders are extremely prevalent, it is unsurprising that efforts

have been made to develop therapeutics for treating MASLD and MASH^{2,8}, including targeting the well-known nutrient sensor mechanistic target of rapamycin complex 1 (mTORC1)⁹. However, due to the complexity of mTORC1's downstream signaling pathways, therapies targeting this pathway have encountered unintended off-target effects. To date, Resmetirom, a thyroid hormone receptor beta (THR- β) agonist, remains the sole therapeutic agent approved by the US FDA for MASH treatment.

¹Department of Nutrition and Health, Key Laboratory of Functional Dairy, China Agricultural University, Beijing, China. ²Department of Health Sciences and Technology, ETH Zurich, Zurich, Switzerland. ³Department of Internal Medicine, Department of Microbiology, UT Southwestern Medical Center, Dallas, TX, USA. ⁴Department of Pharmacology, Toxicology and Therapeutics, The University of Kansas Medical Center, Kansas City, KS, USA. ⁵Department of Internal Medicine, Gastroenterology, Hepatology, Endocrinology and Metabolism, Medical University Innsbruck, Innsbruck, Austria. ⁶College of Food Science and Nutritional Engineering, China Agricultural University, Beijing, China. ⁷These authors contributed equally: Qinqin Ouyang, Jiaqi Su, Yixuan Li.

✉ e-mail: renfazheng@263.net; zhanghaocau@cau.edu.cn; liuronglr010@163.com

Much research into Ras GTPase-activating protein-binding proteins (G3BPs) has focused on their essential roles in the formation of stress granules (protective storage compartments that form inside cells that are experiencing stress, including low nutrient conditions)^{10,11}. However, it is now clear that at least one G3BP (G3BP1) functions in a complex variety of processes, including acting as a helicase (unwinding DNA/DNA, RNA/DNA, and RNA/RNA^{12–14}) and participating in innate immunity through the CGAS/STING pathway, specifically by promoting the DNA binding and activation of CGAS¹⁵. A recent study on various G3BP revealed that G3BP1 resides at the lysosomal surface, where it functions as a tether for the TSC (tuberous sclerosis complex) protein complex, and showed that loss of G3BP1 function phenocopies TSC complex loss in cancer cells and neurons¹⁰.

Autophagy involves the formation of double-membrane structures called autophagosomes, which engulf cytoplasmic material such as proteins, organelles, and lipids for degradation and recycling^{16,17}. Autophagosomes fuse with lysosomes, forming autolysosomes, where the enclosed material is degraded by lysosomal enzymes¹⁸. In the context of liver lipid metabolism, autophagy is known to participate in regulating lipid homeostasis^{6,19}. SNARE proteins mediate the fusion of autophagosomes with lysosomes²⁰. SNARE proteins that have been identified to participate in the fusion of autophagosomes with lysosomes include syntaxin 17 (STX17), and vesicle-associated membrane protein 8 (VAMP8)²¹, among others²². These proteins form a complex that brings the autophagosome and lysosome membranes into close proximity. STX17 is localized to the autophagosome membrane, while VAMP8 is present on the lysosome membrane²³. Previous studies have shown that the extent of autophagic sequestration of lipid droplets (and their subsequent degradation in lysosomes) increases in response to acute lipid stimulus²⁴. Autophagy requires both the autophagosome formation step and the autophagosome-lysosome fusion step^{16,18}. Dysfunction of autophagy has been associated with various metabolic disorders, including MASLD and MASH²⁵.

In the present study, we demonstrate the involvement of G3BP1 in the pathogenesis of MASLD and MASH. Initially, we observed abnormally low levels of G3BP1 in both human MASLD patients and murine models of MASLD and MASH. Subsequently, through various staining techniques, we found that G3BP1 promoted lipid utilization. Consistent with these findings, our experiments involving conditional knockout of G3BP1 in mouse livers showed an exacerbation of high fat diet (HFD)-induced MASLD and high-fat, high-cholesterol (HFHC)-induced MASH. We also identified direct interactions between G3BP1 and the autophagic SNARE proteins STX17 and VAMP8, and found that G3BP1 knockdown resulted in the blockade of autophagosome-lysosome fusion. An RNA-seq analysis indicated that the G3BP1 knockout livers exhibited an increased transcriptional program for de novo lipogenesis. Thus, G3BP1 regulates lipid metabolism in livers by promoting autophagosome-lysosome fusion. This multi-functional protein may be a promising therapeutic target for treating liver lipid disorders.

Results

MASLD patients have reduced levels of Ras GTPase-activating protein-binding protein 1 (G3BP1)

Seeking genes potentially contributing to MASLD pathogenesis, we obtained five RNA-seq datasets for MASLD patients from the GEO database (GSE162694 and GSE126848) and identified differentially expressed genes (DEGs) between patients and healthy control individuals (Fig. 1A). Briefly, the *G3BP1* levels progressively decreased with increasingly severe MASLD activity scores (NAS) (Fig. 1A) and fibrosis scores (Fig. 1B).

We subsequently examined G3BP1 protein expression in liver samples obtained from four MASLD patients and healthy control (HC) individuals. H&E staining and Oil red O staining (Fig. 1C) confirmed the diagnoses of the MASLD patients, while immunohistochemistry

(Fig. 1D) and immunofluorescence (Fig. 1E), and immunoblotting analyses (Fig. 1F) revealed significant reductions in the G3BP1 protein levels in MASLD patients compared to the controls (Fig. 1D–F). The results indicate that the livers of MASLD patients have low levels of G3BP1, suggesting that the dysregulation of G3BP1 function may contribute to the pathophysiology of MASLD.

Murine models of MASLD and MASH display aberrantly low G3BP1 protein levels

We subsequently conducted experiments using murine models of MASLD and MASH and monitored the G3BP1 levels. Briefly, we induced classic models of MASLD and MASH by respectively feeding adult mice (starting at 8 weeks) with a high fat diet (HFD) and a high fat high cholesterol (HFHC) diet, respectively. The MASLD model mice exhibited the expected pathological features including hepatic steatosis (Fig. 1G). Immunoblotting of liver tissue lysates showed a significantly decreased G3BP1 protein level compared to control mice fed a normal control diet (NC) (Fig. 1H). Successful induction of the MASH model was confirmed by increased Sirius red staining of liver sections (Fig. 1I), suggesting increased liver fibrosis. Immunoblotting analysis again showed that liver lysates of the MASH model mice had significantly lower G3BP1 levels compared to non-model control animals (Fig. 1J). These results align with our findings from human MASLD patients and suggest that the dysregulation of G3BP1 function may contribute to the pathophysiology of MASLD and MASH.

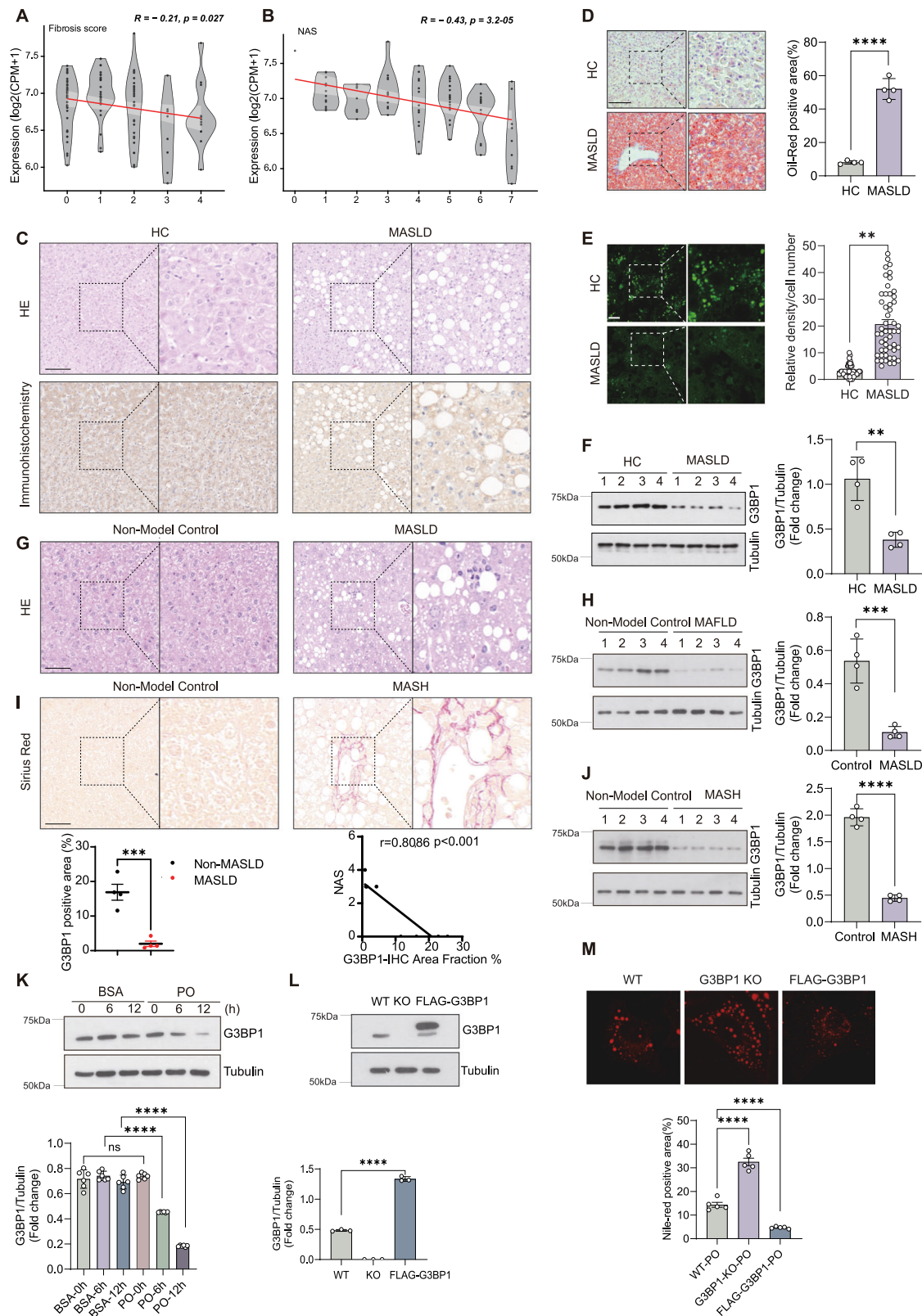
G3BP1 deficiency promotes steatosis

To probe the potential pathogenic impacts of G3BP1, we isolated primary hepatocytes from 8-week-old wild type C57 mice and then exposed the primary hepatocyte cultures to fatty acids (palmitic acid and oleic acid; “PO”) to stimulate lipid accumulation²⁶. Immunoblotting revealed that the hepatocytes exposed to PO had significantly lower G3BP1 levels compared to the BSA-exposed control cultures, with the reduction showing time and dose-dependent (Figs. 1K and S1). We then generated G3BP1 knockout (KO) HepG2 cells via CRISPR-Cas9 editing (Fig. 1L) and exposed the cells to PO. Nile red staining showed that compared to the unedited control cells, the G3BP1 KO cells accumulated significantly more lipids in a dose- and time- dependent manner (Figs. 1M and S1). Conversely, transfecting cells with a construct for FLAG-G3BP1 expression and exposing them to PO led to a significant reduction in lipid content as compared to wild type cells (Figs. 1M and S1). Thus, G3BP1 levels are decreased in hepatocytes in a high-lipid context, and G3BP1 play a critical role in fatty acid and/or lipid metabolism, helping to reduce lipid accumulation in murine livers.

Conditional hepatic knockout of G3BP1 exacerbates HFD-induced MASLD and HFHC-induced MASH

Considering that lipotoxicity is a major cause of MASLD initiation²⁷, we conducted experiments using a 20-week high-fat diet (HFD) feeding regimen to examine the function of G3BP1 in a mouse model of MASLD. We generated liver-specific G3BP1 knockout mice (“LKO”); briefly, G3BP1^{fllox/fllox} mice were crossed with mice carrying Alb-Cre recombinase, and G3BP1^{cre-fllox/fllox} mice or WT control mice were fed either a normal control diet (NC) or HFD for 20 weeks to induce an MASLD model. G3BP1 LKO mice that were fed a HFD exhibited a marked increase in liver size compared to the HFD-fed wild-type (WT) mice (Fig. 2A). Additionally, we observed significant increases in both liver weight and the liver-to-body weight ratio in the HFD-fed G3BP1-LKO mice when compared to the HFD-fed WT mice (Fig. 2B, C).

H&E and Oil red O staining of liver sections were performed to evaluate liver steatosis. The results showed that the HFD-fed G3BP1 LKO mice had a significantly increased number and size of lipid droplets compared to the HFD-fed WT mice (Fig. 2D, E). The livers of HFD-fed G3BP1 LKO mice also had significantly elevated hepatic levels of



cholesterol (TC) (Fig. 2H) and triglycerides (TG) (Fig. 2I) compared to HFD-fed WT mice. Moreover, the HFD-fed G3BP1 LKO mice had multiple characteristic metabolic phenotypes for MASLD, including: significantly poorer performance in both insulin resistance and insulin secretion, as indicated by glucose tolerance (GTT) (Fig. 2F) and insulin tolerance tests (ITT) (Fig. 2G). Additionally, the extent of liver injury was greater in the HFD-fed G3BP1 LKO mice than HFD-fed WT mice as

indicated by the significantly elevated levels of serum alanine aminotransferase (ALT) (Fig. 2J) and aspartate aminotransferase (AST) (Fig. 2K). Taken together, these results support that disrupting G3BP1 function in the liver exacerbates MASLD in mice.

To address potential genetic leakage concerns associated with Alb-Cre recombinase, we injected AAV8-TBG-Cre into G3BP1^{flx/flx} mice to specifically delete *G3bp1* in hepatocytes (here after referred to as

Fig. 1 | Aberrantly low expression of G3BP1 in the livers of MASLD patients and MASLD and MASH. Violin plots for *G3BP1* expression (log2CPM) in the GSE162694 and GSE126848 dataset, in which patients were stratified by fibrosis score (A) or NAS (B); healthy control group: $n = 31$; MASLD group: $n = 112$; The reads were mapped to the Ensembl human (hg19/GRCh37) reference genomes using HISAT2. The gene expression was normalized to CPM (Counts per million reads) using edgeR⁵¹. R package DESeq2⁵² was used to screen the differential expression genes (DEGs) between samples with a criteria of adjusted P value < 0.05 .

C–E Representative liver sections from one healthy control (HC) individual and one MASLD patient. **C** H&E staining was performed to assess liver histopathology (top panel), and immunohistochemistry (IHC) to assess G3BP1 expression in liver tissues from HC and MASLD patients (bottom panel). Scale bars: 50 μm . **D** Representative Oil Red O staining in liver sections. Scale bars: 50 μm . Oil Red O staining quantification was performed using ImageJ. Bar graphs show the mean \pm SEM of the percentage of Oil-red positive areas ($n = 4$ patients per group). Each dot represents the average value from 10 images collected per patient. **** $p < 0.0001$ by two-tailed unpaired t -test. **E** Representative immunofluorescence images (G3BP1 staining) in liver sections from HC and MASLD patients. Scale bars: 10 μm . G3BP1 intensity per cell was quantified by Image-J and are presented as mean \pm SEM (50 cells analyzed from 4 patients per group).

** $p < 0.01$, *** $p < 0.001$ by two-tailed unpaired t -test. **F** Immunoblotting against G3BP1 in extracts from liver samples of 4 healthy controls ($n = 4$) and 4 MASLD patients ($n = 4$). Quantitative result of G3BP1 protein fold change (G3BP1 expression level versus tubulin expression level) in Fig. 1F. Data are presented as mean \pm SEM. ** $p < 0.01$, *** $p < 0.001$ by two-tailed unpaired t -test. **G** Liver samples were collected from C57BL/6J mice fed a standard chow diet (control, $n = 6$) or a high-fat diet (HFD, $n = 6$) for 20 weeks. Histopathological evaluation was performed

through hematoxylin and eosin (H&E) staining of liver sections from control and MASLD model groups. Scale bars, 50 μm . **H** Immunoblotting against G3BP1 in liver tissue lysates from control ($n = 4$) and MASLD model mice ($n = 4$), with quantification of protein levels normalized to Tubulin. Data are presented as mean \pm SEM. * $p < 0.05$, ** $p < 0.01$, *** $p < 0.001$ by two-tailed unpaired t -test. **I** Liver samples from C57BL/6J mice fed a standard chow diet (control, $n = 6$) or high-fat high-cholesterol diet (HFHC, $n = 6$) for 24 weeks were processed for histopathological analysis. Picrosirius red staining of liver sections showing fibrotic progression in MASLD model mice. Data expressed as mean \pm SEM, *** $p < 0.001$ by two-tailed Student's t -test. Scale bars, 50 μm . **J** Immunoblot against G3BP1 in liver tissue lysates from control ($n = 4$) and MASH model mice ($n = 4$), with quantification of protein levels normalized to Tubulin. Data expressed as mean \pm SEM. **** $p < 0.0001$ by two-tailed unpaired t -test. **K** Primary hepatocytes from C57BL/6J mice (8-week male, $n = 6$ biologically independent samples) were treated with palmitic acid and oleic acid (PO) for indicated durations (0, 6, 12 h). Immunoblot of G3BP1 with Tubulin loading control. Densitometric quantification normalized to Tubulin. Data expressed as mean \pm SEM. * $p < 0.05$, ** $p < 0.01$, *** $p < 0.001$ by two-way ANOVA. **L** FLAG-G3BP1 overexpression and CRISPR/Cas9-mediated knockout in HepG2 cells, with immunoblot analysis using anti-G3BP1 antibodies showing engineered protein expression and endogenous depletion, normalized to Tubulin; ($n = 3$, three independent experiments). **** $p < 0.0001$ by one-way ANOVA. **M** Representative images of Nile red staining in WT, FLAG-G3BP1 overexpression, and G3BP1 KO HEPG2 cells treated with PO for 12 h. Scale bars, 5 μm . Percentage of Nile red positive area was quantified by Image-J. All values are presented as mean \pm S.E.M. ($n = 5$). Each dot represents the average value from 6 images collected per independent experiment. **** $P < 0.0001$, analysis of one-way ANOVA.

G3BP1 HKO (hepatocyte-specific knockout) and fed either a NC or HFD to induce MASLD. Notably, both G3BP1 LKO and G3BP1 HKO mice exhibited consistent phenotypic exacerbation compared to WT mice fed with HFD.

The observed phenotypes comprised marked hepatic enlargement (Fig. S2A). Histological analyses via H&E and Oil red O staining demonstrated a significant expansion in both the quantity and dimensions of lipid droplets relative to WT counterparts (Fig. S2B, C). Biochemical assessments revealed substantially augmented hepatic levels of TC (Fig. S2D) and TG (Fig. S2E) in genetically modified mouse livers. The serum levels of AST (Fig. S2F), ALT (Fig. S2G) and notably greater fat mass accumulation (Fig. S2H) were significantly elevated in knockout mice compared to WT controls. These consistent results across two independent knockout strategies confirm that hepatic G3BP1 disruption exacerbates MASLD.

Considering that MASH represents an advanced stage of MASLD², we conducted a study to examine the role of G3BP1 in a mouse model of MASH induced by feeding the mice with an HFHC diet for 24 weeks. The HFHC fed G3BP1 LKO mice exhibited significantly increased liver weight (Fig. 3A) and liver-to-bodyweight ratio (Fig. 3B) compared to the WT MASH model mice. Additionally, hepatic steatosis and fibrosis was more severe in the G3BP1 LKO mice compared with WT mice as indicated by H&E (Fig. 3C) and Sirius red staining (Fig. 3D). Additionally, the G3BP1 LKO mice exhibited significantly poorer performance in both glucose tolerance and insulin tolerance tests (Fig. 3E, F), as well as significantly elevated levels of AST and ALT (Fig. 3G, H) compared to the WT mice. The hepatic levels of TC and TG levels in HFHC-fed G3BP1 LKO mice were also significantly increased compared to HFHC-fed WT mice (Fig. 3I, J). Consistent with the histological findings, quantitative PCR analysis demonstrated marked upregulation of fibrogenic genes (*Col1a1*, *Acta2*, *Tgfb*, and *Timp1*) and inflammatory markers (*TNF- α* and *IL-6*) in HFHC-fed G3BP1 LKO livers compared to WT mice (Fig. 3K–P). Thus, loss of hepatic G3BP1 exacerbates the pathogenesis of MASLD and MASH in mice.

Autophagosome-lysosome fusion is disrupted in G3BP1 LKO MASLD model

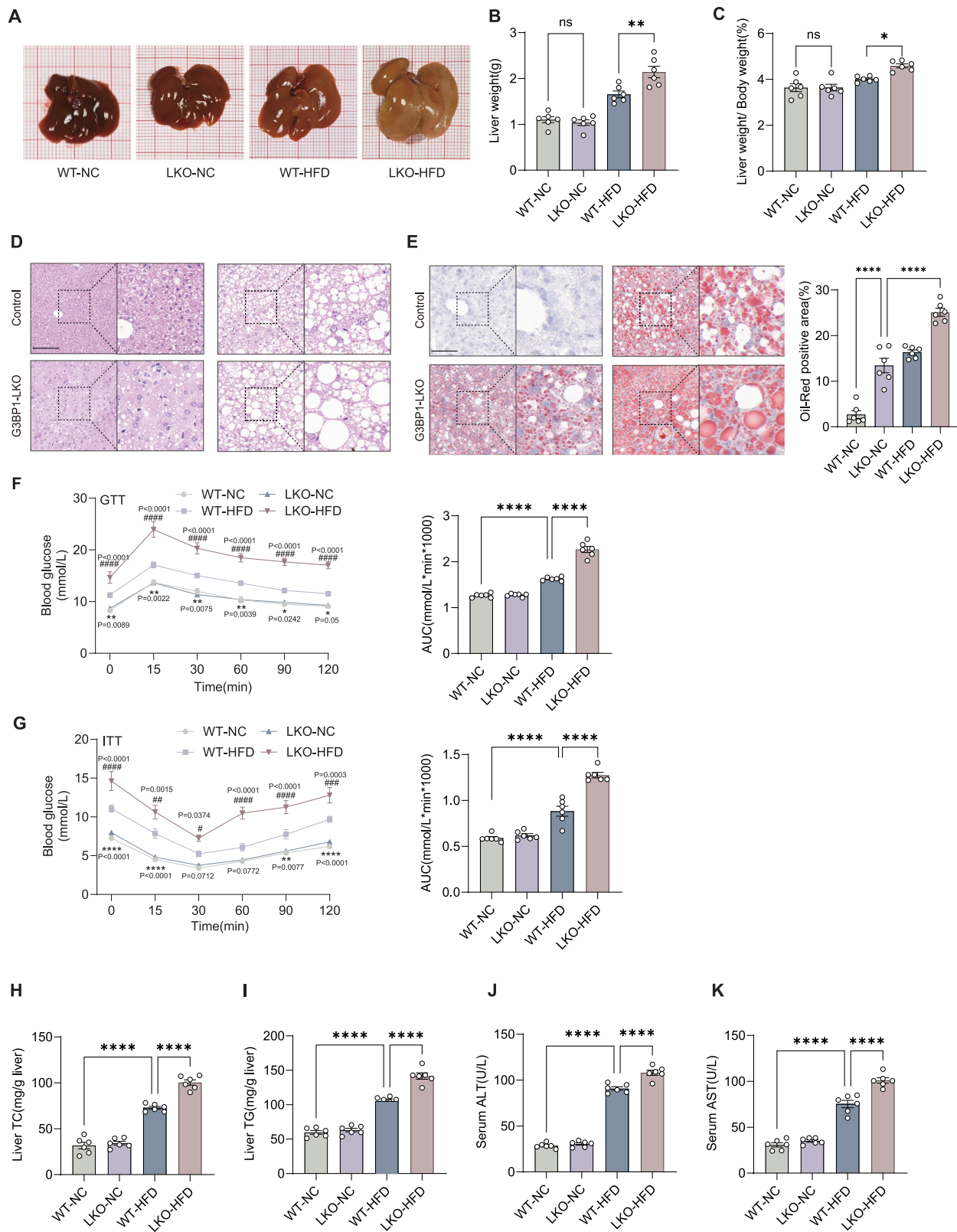
Since autophagy is known to regulate liver lipid homeostasis²⁸, we investigated its potential role in the worsening development of MASLD

in the G3BP1 LKO mice. This was done by staining liver sections with LC3, a commonly used marker for autophagic membranes²⁹. The LC3 signal intensity was significantly higher in the HFD-fed G3BP1 LKO mouse livers than the HFD-fed WT mice (Fig. 4A). Consistent with the immunostaining, immunoblotting analysis of liver tissues showed significantly increased levels of LC3-II in HFD-fed G3BP1 LKO mouse livers compared to HFD-fed WT mice (Fig. 4B). Defective fusion of autophagosome with lysosome or impaired lysosomal functions can often lead to accumulation of LC3-II. Thus, increased LC3-II levels in HFD-fed G3BP1 LKO mice suggests that hepatic deletion of G3BP1 may inhibit autophagy in the context of MASLD.

To identify the specific step of autophagy affected by G3BP1 deletion, we carried out autophagic flux assays *in vitro*³⁰. Compared with the scramble control HepG2 cells, the turnover rates of both LC3-II were significantly reduced in G3BP1 knockdown cells (Fig. 4C, D). To validate this defect *in vivo*, we first conducted ultrastructural analysis via transmission electron microscopy. Remarkably, HFD-fed G3BP1 LKO livers showed a marked increase in autophagosome density compared to WT littermates (Fig. 4E), suggesting loss of G3BP1 lead to the accumulation of autophagosomes likely due to impaired fusion of autophagosomes with lysosomes. To functionally confirm this impairment, we utilized an AAV8-delivered mRFP-GFP-LC3 reporter system. Confocal microscopy revealed a dramatic increase in yellow puncta (GFP+/RFP+ vesicles, indicative of unfused autophagosomes) in HFD-fed G3BP1-LKO mouse livers compared to HFD-fed WT mice (Fig. 4E), further supporting loss of hepatic G3BP1 may impair fusion of autophagosomes with lysosomes.

G3BP1 interacts directly with the SNARE proteins STX17 and VAMP8

Previous studies have established that autophagosome-lysosome fusion is regulated by a group of proteins called SNAREs (Soluble NSF Attachment Protein Receptors)—membrane-associated proteins that mediate membrane fusion events. The process of autophagosome-lysosome fusion begins with the recruitment of specific SNARE proteins (STX17 to the autophagosome membrane and VAMP8 on the lysosomal membrane), which subsequently promote fusion, allowing the cargo within the autophagosomes to be degraded in



lysosomes^{23,31}. To explore how G3BP1 promotes autophagosome-lysosome fusion, we performed co-immunoprecipitation (co-IP) with various cell lysates to examine potential interactions between G3BP1 and SNARE proteins. Briefly, co-IP of cells co-expressing HA-G3BP1 and FLAG-VAMP8 revealed an interaction between HA-G3BP1 and FLAG-VAMP8 (Fig. 5A), as well as an interaction between FLAG-G3BP1 and STX17 (Fig. 5B). Subsequent experiments with antibodies against

SNAREs showed that FLAG-G3BP1 interacts with STX17 and VAMP8 (Fig. 5C).

We further analyzed the direct interaction between G3BP1 and SNARE proteins by purifying recombinant VAMP8, STX17, and G3BP1 from *E. coli*. Pull-down assays showed that G3BP1 binds directly with STX17 and with VAMP8 (Fig. 5D, E). To evaluate the pathophysiological relevance of these interactions, we analyzed hepatic tissues from

Fig. 2 | Conditional hepatic deletion of G3BP1 exacerbates HFD-induced MASLD. **A** Liver gross morphology of wild-type (WT) and G3BP1 LKO mice fed normal chow (NC) or high-fat diet (HFD) for 20 weeks ($n = 6$), imaged by Nikon SMZ25 stereomicroscope. Liver weight (**B**) and liver-to-body weight ratio (**C**) of WT and G3BP1 LKO mice fed normal chow (NC) or HFD for 20 weeks ($n = 6$ mice per group). All values are presented as means \pm S.E.M. Statistical analysis was performed using two-way ANOVA followed by Sidak's multiple comparisons test (two-sided). $^*P < 0.05$; $^{**}P < 0.01$. **D** H&E-stained liver sections from WT and G3BP1 LKO mice fed NC or HFD for 20 weeks ($n = 6$), imaged using Leica microscope. Scale bars: 50 μ m. **E** Representative images of liver sections stained with Oil red staining from G3BP1 LKO and WT mice that were fed NC or HFD for a duration of 20 weeks ($n = 6$ mice per group). Scale bars, 50 μ m. The right panels depict the percentage of Oil red positive area of liver sections from indicated groups, analyzed using ImageJ. Data are presented as means \pm S.E.M. ($n = 6$ mice per group). Each dot represents the average value from 10 images collected per mice. $^{****}P < 0.0001$ by two-way ANOVA followed by Sidak's post hoc test for multiple comparisons (two-sided). **F** Glucose tolerance tests (GTT) were performed in G3BP1 LKO and WT mice after NC or HFD consumption, and the corresponding AUC values were calculated ($n = 6$ mice per group). All values are presented as means \pm S.E.M. Statistical analysis was

performed using two-way ANOVA followed by Sidak's post hoc test for multiple comparisons (two-sided). Exact p values are shown in the figure. *: WT-NC vs. WT-HFD; #: LKO-HFD vs. WT-HFD. **G** Insulin tolerance test (ITT) assays data for the non-model control and MASLD model G3BP1 LKO and WT mice, and the AUC (area under the curve) values were calculated accordingly ($n = 6$ mice per group). All values are presented as means \pm S.E.M. Statistical analysis was performed using two-way ANOVA followed by Sidak's post hoc test for multiple comparisons (two-sided). Exact p values are shown in the figure. *: WT-NC vs. WT-HFD; #: LKO-HFD vs. WT-HFD. Hepatic total cholesterol (TC, **H**) and triglycerides (TG, **I**) quantified by enzymatic colorimetric assays in WT and G3BP1 LKO mice under NC or MASLD model induced by HFD for 20 weeks ($n = 6$ mice per group); All values are presented as means \pm S.E.M. $^{****}P < 0.0001$, analysis of two-way ANOVA followed by Sidak's post hoc test for multiple comparisons (two-sided). Serum alanine aminotransferase (ALT, **J**) and aspartate aminotransferase (AST, **K**) concentrations quantified by enzymatic assays in WT and G3BP1 LKO mice under NC or MASLD model induced by HFD for 20 weeks ($n = 6$ mice per group); All values are presented as means \pm S.E.M. $^{****}P < 0.0001$, analysis of two-way ANOVA followed by Sidak's post hoc test for multiple comparisons (two-sided).

experimental MASLD/MASH mice. Co-IP assays revealed significantly reduced G3BP1-STX17 and G3BP1-VAMP8 interactions in the MASLD/MASH group compared to controls (Fig. 5F, G). This impaired interaction may underlie the defective autophagosome-lysosome fusion observed in our MASLD/MASH mouse models.

Moreover, we investigated the intracellular distribution of STX17, VAMP8, the lysosome marker LAMP2, as well as their colocalization with G3BP1 upon treatment with the autophagy inducer Torin1. Upon initiation of autophagy, G3BP1 colocalized on autolysosomes (indicated by VAMP8 and STX17 and by STX17 and LAMP2) (Fig. 5F–H). These findings support a plausible model wherein G3BP1 regulates autophagosome-lysosome fusion through its colocalization and direct interactions with the SNARE proteins STX17 and VAMP8.

Hepatic knockout of G3BP1 promotes de novo lipogenesis

Given our observation that conditional hepatic knockout of G3BP1 exacerbates the development of MASLD and MASH, we explored the potential impacts of G3BP1 in lipid metabolism by performing RNA-seq and qPCR from liver tissues of HFD and HFHC-fed G3BP1 LKO and WT mouse livers. RNA-seq heatmap analysis revealed significantly increased levels of mRNA transcripts of de novo lipogenesis genes in the G3BP1 LKO mice compared to WT mice (Fig. 6A, B). Quantitative PCR analysis showed significantly increased levels of acyl-CoA synthetase short chain family member 2 (*Acsc2*)³², carbohydrate response element binding protein 1 (*Chrebp1*)³³, acetyl-CoA carboxylase alpha (*Acaca*)³⁴, sterol regulatory element-binding protein 1C (*Srebp1c*)³⁵, and stearoyl-CoA desaturase-1 (*Scd1*)³⁶ in HFD and HFHC-fed G3BP1 LKO mice compared to WT mice (Fig. 6C, D). Furthermore, immunoblotting analysis also showed significantly increased levels of SREBP1, ACLY, and ACS2 in the livers of HFD and HFHC-fed G3BP1 LKO mice compared to WT mice (Fig. 6E, F). Together, these data indicate that loss of hepatic G3BP1 induces a transcriptional program for de novo lipogenesis in the mouse liver.

G3BP1 is required for TFE3 nuclear translocation to suppress lipogenesis

A recent study reported that hepatocyte-specific genetic deletion of FLCN in adult mice provided protection against both MASLD and MASH, and showed that these protective effects are dependent on the nuclear translocation of Transcription factor E3 (TFE3), a master transcriptional regulator with widespread impacts on processes including (but not limited to) lysosome biogenesis and lipolysis^{37–40}. Given our finding that G3BP1 LKO mice exacerbates MASLD and MASH development and considering our RNA-seq data for lipid metabolism genes, we speculated that G3BP1 may also regulate TFE3 activity.

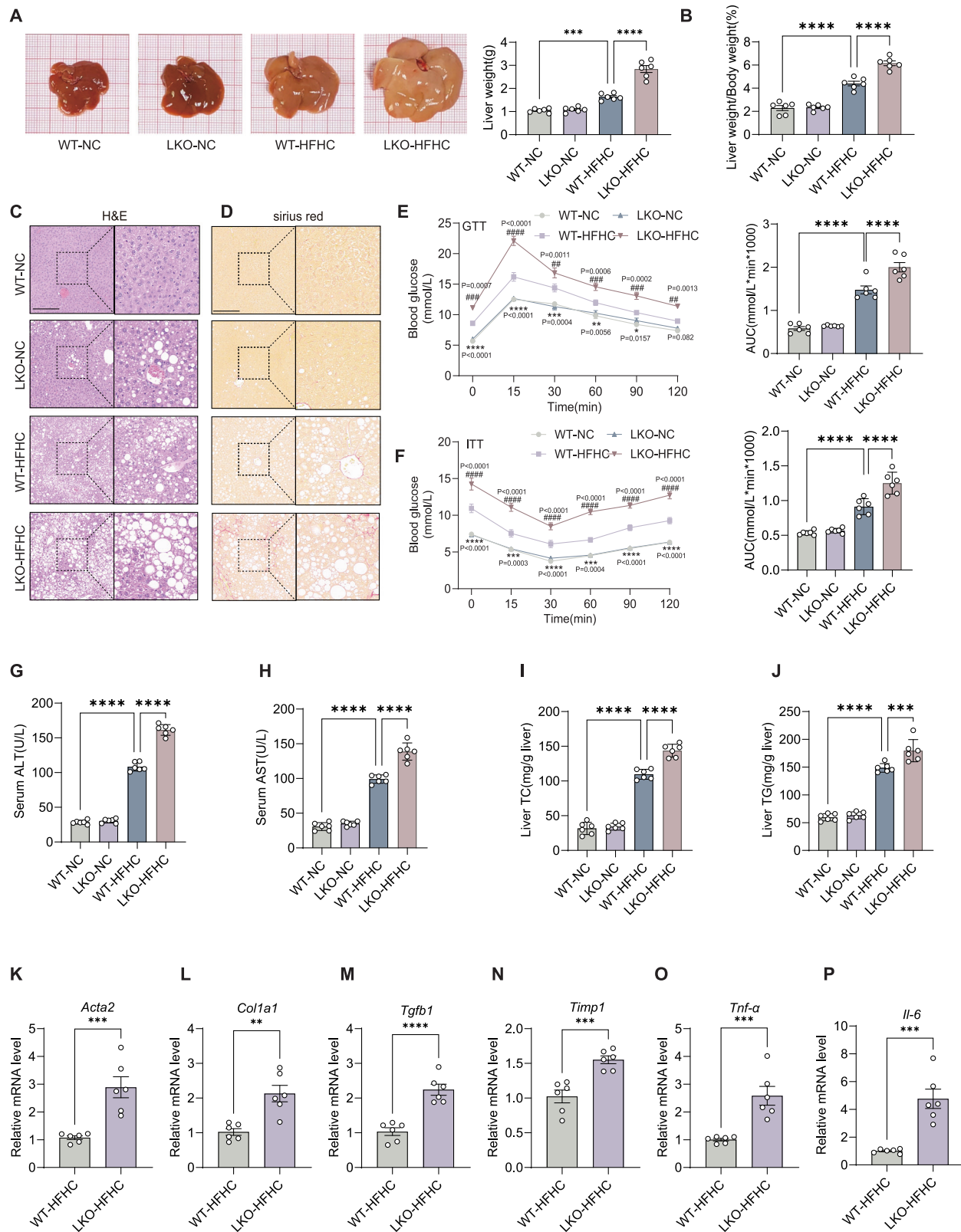
Pursuing this, we examined TFE3 activation (*i.e.*, nuclear translocation) in HFD-fed WT and G3BP1 LKO mice. Immunofluorescence staining revealed significantly reduced nuclear accumulation of TFE3 in G3BP1 LKO hepatocytes compared to WT controls (Fig. 7A). This was corroborated by cellular fractionation assays showing dramatically reduction of nuclear TFE3 protein in G3BP1 LKO mouse livers (Fig. 7B). INSIG2 protein levels dramatically decreased, accompanied by increased levels of mature SREBP1 in G3BP1 LKO mice (Fig. 7C).

To establish causality, we performed rescue experiments by delivering AAV8-TFE3 to overexpress TFE3 in HFD-fed G3BP1 LKO mice. Overexpression of TFE3 diminished lipid droplet area (Oil Red O; Fig. 7D), ameliorated hepatocyte ballooning (H&E Fig. 7D) as well as decreased hepatic levels of TG and TC in HFD-fed G3BP1 LKO mice (Fig. 7E, F). Moreover, overexpression of TFE3 also significantly decreased serum ALT and AST activities in HFD-fed G3BP1 LKO mice (Fig. 7G, H). These findings collectively demonstrate that G3BP1 sustains TFE3 nuclear translocation to restrain lipogenesis and hepatocyte injury to protect against the pathogenesis of MASLD.

Discussion

In the present study, we found that human MASLD patients and murine models of both MASLD and MASH display aberrantly low levels of G3BP1. Analysis of human hepatocytes showed that G3BP1 promotes lipid utilization, and we found that conditional hepatic knockout of G3BP1 exacerbates HFD-induced and HFHC-induced MASH, specifically by inhibiting autophagosome-lysosome fusion. We also found that hepatic G3BP1 is required for TFE3's (activating) nuclear translocation. Liver conditional knockout G3BP1 inhibits TFE3 nuclear translocation, thereby inducing a de novo lipogenesis transcriptional program. Our study thus reveals G3BP1 as a target for developing treatments for MASLD.

While the large majority of previous research into the G3BPs has centered on stress granules^{41–43}, multiple studies have demonstrated that these proteins exert a diverse array of cellular-context-dependent functions, including in tethering the TSC complex to lysosomes¹⁰, functioning as an ATP- and magnesium-dependent helicase¹², and promoting CGAS/STING signaling⁴⁴, among others⁴⁵. In this context, it is particularly notable that our study revealed another interaction between G3BP1 and a lysosomal-membrane-localized SNARE protein (VAMP8). Here, we found that G3BP1 interacts with and is colocalized with both STX17 and VAMP8 in vivo and in vitro, and our discovery that reduced G3BP1 levels inhibited autophagosome-lysosome fusion helps explain the accumulation of lipids in hepatocytes, murine MASLD and MASH models, and human MASLD patients. It thus appears that G3BP1 engages in a set of interactions with lysosome components, and it will



be interesting to experimentally delineate the various nutrition-induced context(s)—and potentially informative order of engagements—through which G3BP1 contributes to autophagic degradation and lipid recycling. To exclude mitochondrial contributions, we also determined the gene expression of mitochondria beta oxidation genes and investigated the mitochondrial ultra-structure via EM analysis, we did not find significant changes on these gene

expression (Fig. S3A and B) and mitochondria morphology in G3BP1 LKO mice (Fig. S3C).

Increased nuclear translocation of TFE3 has been reported to promote the transcription of multiple genes with known functions in metabolic regulators⁴⁶. Our finding of exacerbated disease phenotypes upon conditional liver knockout of G3BP1 in both HFD-induced MASLD and HFHC-induced MASH mouse models motivated our follow-up

Fig. 3 | Conditional hepatic deletion of G3BP1 exacerbates HFHC-induced MASH. **A** Gross hepatic morphology and liver weight quantification (right panels) of WT and G3BP1 LKO mice fed NC or high-fat high-cholesterol diet (HFHC) for 24 weeks ($n = 6$ mice per group). All values are presented as means \pm S.E.M. $*P < 0.05$; $****P < 0.0001$, analysis of two-way ANOVA followed by Sidak's post hoc test for multiple comparisons (two-sided). **B** The liver/body weight ratio of G3BP1 LKO and WT mice after NC or HFHC consumption for 24 weeks ($n = 6$ mice per group). All values are presented as means \pm S.E.M. $****P < 0.0001$, $***P < 0.001$, analysis of two-way ANOVA followed by Sidak's post hoc test for multiple comparisons (two-sided). **C** Representative H&E-stained liver sections from WT and G3BP1 LKO mice fed NC or HFHC for 24 weeks ($n = 6$), imaged by Leica microscope (scale bars: 50 μ m). **D** Sirius red-stained liver sections from WT and G3BP1 LKO mice fed NC or HFHC for 24 weeks ($n = 6$), imaged by Leica microscope (scale bars: 50 μ m). **E** Intraperitoneal glucose tolerance tests (GTT) in WT and G3BP1 LKO mice fed NC or HFHC for 24 weeks ($n = 6$ mice per group), with blood glucose monitored at 0/15/30/60/90/120 min and area under curve (AUC) calculated by trapezoidal method. All values are presented as means \pm S.E.M. Statistical analysis was performed using two-way ANOVA followed by Sidak's post hoc test for multiple comparisons (two-sided). Exact p values are shown in the figure. *: WT-NC vs. WT-HFHC; #: LKO-HFHC vs. WT-HFHC. **F** Intraperitoneal insulin tolerance tests (ITT) in

WT and G3BP1 LKO mice fed NC or HFHC for 24 weeks ($n = 6$ mice per group), with blood glucose monitored at 0/15/30/60/90 min and area under curve (AUC) calculated by trapezoidal method; All values are presented as means \pm S.E.M. Statistical analysis was performed using two-way ANOVA followed by Sidak's post hoc test for multiple comparisons (two-sided). Exact p values are shown in the figure. *: WT-NC vs. WT-HFHC; #: LKO-HFHC vs. WT-HFHC. **ALT (G)** and **AST (H)** concentrations measured in WT and G3BP1 LKO mice fed NC or HFHC for 24 weeks ($n = 6$ mice per group). All values are presented as means \pm S.E.M. $****P < 0.0001$, analysis of two-way ANOVA followed by Sidak's post hoc test for multiple comparisons (two-sided). The liver **TC (I)** and **TG (J)** levels of the G3BP1 LKO and WT mice fed normal control diet or HFHC ($n = 6$ mice per group). All values are presented as means \pm S.E.M. $****P < 0.0001$, analysis of two-way ANOVA followed by Sidak's post hoc test for multiple comparisons (two-sided). **K–P** Quantitative RT-PCR analysis of fibrogenesis-related genes (*Acta2*, *Col1a1*, *Tgfb1*, *Timp1*) and inflammatory markers (*Tnf- α* , *Il6*) in liver tissues from WT and G3BP1 LKO mice with MASH induced by 24-week HFHC diet ($n = 6$ mice per group). Gene expression was normalized to *Gapdh* and is presented as mean \pm S.E.M. Statistical significance was assessed using unpaired two-tailed Student's t -test. Exact p values are as follows: (K) *Acta2*, $***P = 0.0008$; (L) *Col1a1*, $**P = 0.0015$; (M) *Tgfb1*, $****P < 0.0001$; (N) *Timp1*, $***P = 0.0007$; (O) *Tnf- α* , $***P = 0.0010$; (P) *Il6*, $***P = 0.0003$.

studies which ultimately showed an altered transcriptional program for de novo lipogenesis (including *Srebp1c*, *Acsc2*, *Acaca*, *Chrebp*, and *Scd1*) that can be plausibly explained by our finding that G3BP1 regulates the activating nuclear translocation of TFE3. It will be interesting to examine G3BP1's regulation of TFE3 translocation in additional nutrient contexts and to evaluate whether G3BP1 engages with any other proteins with known functions in mTORC1-mediated regulation of TFE3.

Recalling that there are only one US FDA-approved therapies for MASH, and given the increasing prevalence of MASLD and MASH worldwide⁴⁷, it is clear that effective treatment options would be welcomed by clinicians. Our study has implications regarding the diagnosis and monitoring MALFD as well as for potential G3BP1-targeting based interventions for MASLD and MASH. That is, our finding of aberrantly low G3BP1 levels in liver samples of MASLD patients suggests that this protein can be added to the set of informative markers that clinicians can use—currently including plasma cytokeratin 18⁴⁸—when diagnosing and managing MASLD cases. Regarding targeting G3BP1, it will be interesting to explore how interventions that simultaneously manage liver lipid load (ostensibly via diet) and promote autophagy for lipid degradation (ostensibly using an agonist or strategy to increase G3BP1's half-life) may confer benefit in for example helping reverse MAFLD pathology and/or protecting against progression of MAFLD to MASH, cirrhosis, and cancer.

Methods

Human transcriptomic analysis

The public human MASLD patient sample data were obtained from the NCBI Gene Expression Omnibus (GSE162694 and GSE126848)⁴⁹. The GEOquery R package was employed to parse sample phenotype information, filtering samples with complete NAS (0–8) and fibrosis stage (0–4) annotations based on criteria from the original publication. The RNA-seq data were mapped to hg19 reference genome (UCSC assembly) using HISAT2 (v2.2.1)⁵⁰. Gene expression values were normalized to CPM (Counts per million reads) using edgeR (v4.4.2). Principal component analysis (PCA) revealed batch effects, which were corrected via ComBat-seq applied to raw count matrices (covariate: GSE series identifier)⁵¹. The R package DESeq2 (v1.46.0)⁵² was used to identify the differentially expressed genes (DEGs) between samples. All participants gave informed consent.

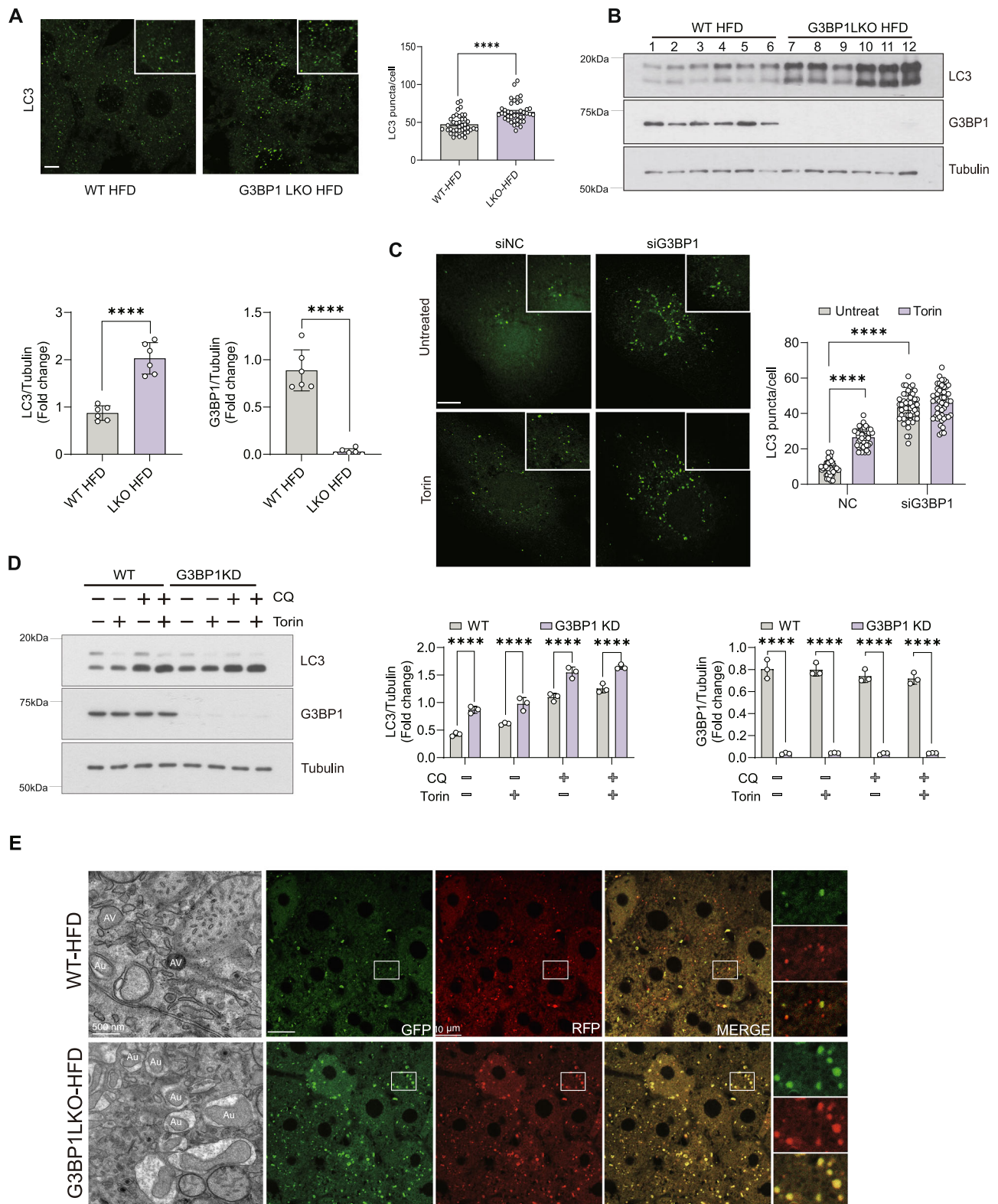
Cell culture

The human cell lines HEPG2 and HEK293T were obtained the American Type Culture Collection (ATCC). The cell lines were tested for

mycoplasma contamination, and the results came back negative. Cells were cultured in Dulbecco's Modified Eagle's Medium (DMEM) (Cytiva, SH30022.01) with 10% Fetal Bovine Serum (FBS) (Thermo Fisher Scientific, A5256701) and 1% Penicillin-Streptomycin (P/S) (Beyotime, C0222) solution, and were maintained at 37 °C in a humidified incubator with 5% CO₂. For Torin1 treatment, cells were exposed to a concentration of 100 nM Torin1 for 2 h. For chloroquine (CQ) treatment, cells were treated with a concentration of 10 μ M CQ for 2 h. To create an in vitro model of hepatic steatosis, mouse primary hepatocytes were exposed to palmitic acid (PA; 0.5 mM; Sigma-Aldrich, P0500) and oleic acid (OA; 1.0 mM; Sigma-Aldrich, O-1008) dissolved in 0.5% fatty acid-free BSA at the specified concentrations. For experiments involving amino acid deprivation or restimulation, the cells were treated following the previously mentioned procedure⁵³. In short, the cells were incubated in amino acid-free DMEM for 50 min and subsequently restimulated with amino acids for 10 min.

Animal experiments

C57BL/6J mice (8 weeks of age) were purchased from Beijing Vital River Laboratory Animal Technology Co. Ltd. The animals were housed 3–5 animals per cage, and kept in a pathogen-free environment, with temperature control set at 22–24 °C, and subjected to a 12-h light/dark cycle. G3BP1^{fllox/flox} mice were generated using a CRISPR/Cas9 system in the C57BL/6J background. G3BP1 LKO mice were created by crossing of G3BP1^{fllox/flox} mice with mice carrying Alb-Cre recombinase. Male mice were fed a high fat diet (HFD) (protein, 20%; fat, 60%; carbohydrates, 20%; HUAFUKANG Bioscience, H10060) or a high fat high cholesterol (HFHC) (protein, 17%; fat, 41%; carbohydrates, 42%; cholesterol, 0.15%; HUAFUKANG Bioscience, H10141) to establish the MASLD or MASH models, respectively. G3BP1 LKO male mice were administered AAV8-TBG-Cre (5×10^{11} viral genomes/mouse) or AAV8-control (5×10^{11} viral genomes/mouse) via tail vein injection at 7 weeks of age, both suspended in 200 μ L PBS. Starting at 8 weeks of age, cohorts were fed either the ND or HFD for 20 weeks. For TFE3 expression, 8-week-old G3BP1 LKO male mice were injected via tail vein with AAV8-Control or AAV8-TBG-TFE3 (5×10^{11} viral genomes/mouse) and maintained on HFD for 20 weeks. For mRFP-GFP-LC3 autophagic flux assay, male WT or G3BP1 LKO mice received tail vein injections of AdV-TBG-mRFP-GFP-LC3 (1×10^{10} PFU, VectorBuilder) after 20 weeks of HFD feeding. Livers tissues were perfusion-fixed with 4% paraformaldehyde (PFA) (Sigma-Aldrich, 158127), and sequentially cryoprotected in 15% sucrose (Sigma-Aldrich, S9378) at 4 °C for 24 h, followed by 30% sucrose at 4 °C for additional 24 h. Tissues were then embedded in OCT



compound (Sakura, 4583), snap-frozen in liquid nitrogen. Following cryoprotection, tissues embedded in OCT compound were sectioned at a thickness of 5 μ m using a Cryotome (Leica, CM3050S). Confocal imaging was performed under standardized parameters: 488 nm/500–550 nm (GFP) and 561 nm/570–620 nm (mRFP) channels, 2.5% laser power, and matched detector gains. All animal experiments were approved by the Institutional Animal Care and Utilization Committee of China Agricultural University.

Liver histopathology

For Paraffin embedding, Liver tissues were fixed in 10% formaldehyde overnight, followed by gradient ethanol dehydration (70% for 60 min, 80% for 60 min, 95% for 45 min, 100% I for 15 min, 100% I for 10 min) and xylene clearing (2 \times 10 min) using an automated tissue processor. After dehydration, tissues were first equilibrated in a 1:1 soft paraffin-xylene mixture (30 min at 65 $^{\circ}$ C), followed by two pure paraffin infiltrations (soft paraffin [melting point: 52–54 $^{\circ}$ C] 30 min; hard paraffin

Fig. 4 | The fusion between autophagosomes and lysosomes is impaired in the G3BP1 LKO MASLD model. **A** Representative immunofluorescence staining images of LC3 (green) of the liver sections from G3BP1 LKO and WT mice fed with HFD for 20 weeks ($n = 6$ mice per group). The right panel shown the quantification result of LC3 puncta number per cell. Scale bars: 5 μm . All values are presented as means \pm SD (at least 40 cells analyzed from 6 mice per group). Statistical significance was assessed using unpaired two-tailed Student's *t*-test. **** $P < 0.0001$. **B** Western blot analysis of LC3 and G3BP1 in liver lysates from WT and G3BP1 LKO mice fed HFD for 20 weeks ($n = 6$ mice per group). The lower panels shown the densitometric quantification of LC3 and G3BP1 normalized to Tubulin. Data expressed as mean \pm SEM. Statistical significance was assessed using unpaired two-tailed Student's *t*-test. **** $P < 0.0001$. **C** HEPG2 cells were transfected with either control siRNA or siG3BP1 for 48 h, followed by incubation in standard culture medium or exposure to 100 nM Torin1 for 2 h. LC3 was assessed through immunofluorescence staining using an LC3-specific antibody, with quantitative analysis (right panel) reflecting LC3-positive puncta counts per cell under fluorescence

microscopy. Scale bars: 10 μm . All values are presented as means \pm S.E.M (at least 50 cells analyzed per group across three biological replicates). **** $P < 0.0001$, analysis of two-way ANOVA followed by Sidak's post hoc test for multiple comparisons (two-sided). **D** HEPG2 cells transfected with control siRNA or siG3BP1 were treated with 100 nM Torin1 \pm 20 mM chloroquine (CQ) for 2 h followed by western blot analyses. The right panels shown the quantification result of LC3II and G3BP1 intensity normalized to tubulin. Data are presented as means \pm S.E.M ($n = 3$, three independent experiments). **** $P < 0.0001$, analysis of unpaired two-tailed Student's *t*-test.

E Representative confocal images of AAV-delivered mRFP-GFP-LC3 fluorescence in HFD-fed WT and G3BP1 LKO livers. Yellow puncta (GFP+/RFP+ co-localization) signify impaired autophagosome-lysosome fusion. Transmission electron microscopy (TEM) of liver sections from HFD-fed WT and G3BP1 LKO mice, revealing markedly increased autophagosome density in G3BP1 LKO hepatocytes, indicative of defective autophagic flux. Scale bars, 10 μm . Each experiment was repeated independently at least three times.

[melting point: 56–58 $^{\circ}\text{C}$], 3 h at 65 $^{\circ}\text{C}$). After infiltration, tissues were oriented in pre-warmed molds, solidified on a 4 $^{\circ}\text{C}$ cold plate, and trimmed. Sections (5 μm) were cut using a rotary microtome (Leica, RM2255), floated on a 45 $^{\circ}\text{C}$ water bath, and mounted on slides for drying (65 $^{\circ}\text{C}$, 2 h). For OCT embedding, fixed tissues were cryoprotected in 15% sucrose (Sigma-Aldrich, S9378) at 4 $^{\circ}\text{C}$ for 24 h, followed by 30% sucrose at 4 $^{\circ}\text{C}$ for an additional 24 h. Tissues were then embedded in OCT compound (Sakura, 4583), snap-frozen in liquid nitrogen, and storage at -80°C . Before sectioning, frozen blocks were brought up to about -20°C , then sectioned at 5 μm on a Cryotome (Leica, CM3050S). Deparaffinization involved sequential immersion in xylene I/II (20 min each), absolute ethanol I/II (5 min each), 95% ethanol (5 min), 85% ethanol (5 min), 70% ethanol (5 min), and triple rinses in distilled water. H&E staining was performed on 5 μm thickness Paraffin sections that were prepared and deparaffinized to water with Gill's modified hematoxylin (Solarbio, G1120-1) for 5 min, followed by rinsing in running tap water. Sections were then differentiated with acid alcohol for 30 s, immersed in tap water for 15 min, and counterstained with eosin (Solarbio, G1120-2) for 2 min. After rinsing with running tap water, sections were dehydrated in a graded ethanol series (95% ethanol I, 1 min; 95% ethanol II, 1 min; 100% ethanol I, 1 min; 100% ethanol II, 1 min), cleared in xylene (I, 1 min; II, 1 min), and mounted using a neutral resinous medium for microscopic observation. Sirius red staining (Solarbio, G1472) was performed on 5 μm thickness Paraffin sections that were prepared and deparaffinized to water. Tissues were pre-stained with freshly prepared ferric hematoxylin for 5 min, then rinsed with distilled water for 10–20 s to remove excess stain, followed by Sirius red staining for 10 min. Sections were rapidly rinsed in distilled water to remove excess staining solution. Dehydration was performed using a graded ethanol series starting from 75%, followed by clearing in xylene and mounting with a neutral resinous medium. Oil Red O staining (Solarbio, G1262) was performed on thawed OCT sections (5 μm thickness). The sections were first incubated with 60% isopropanol for 30 s for differentiation, followed by staining with freshly prepared Oil Red O solution for 10 min. Excess stain was removed, followed by differentiation in 60% isopropanol for 10–20 s until the background appeared clear. Sections were then rinsed with distilled water 2–5 times until no excess staining solution was released. Mayer's hematoxylin was applied for nuclear counterstaining for 2 min, followed by rinsing with distilled water 3 times. Coverslips were mounted with glycerin gelatin, and stained sections were observed under a microscope (Leica, DFC450C)^{54,55}.

Primary hepatocyte isolation

Eight-week-old male C57BL/6J mice were fed a standard diet. The portal vein was cannulated using a 24G IV catheter (Terumo, SR-OX2419CA) and secured with a 4-0 silk suture. Liver perfusion was initiated with pre-warmed (37 $^{\circ}\text{C}$) Liver Perfusion Medium (Thermo

Fisher Scientific, 17701-038) at a flow rate of 5 mL min⁻¹ via a peristaltic pump, followed by Liver Digestion Medium (Thermo Fisher Scientific, 17701-034). During perfusion, intermittent pressure was applied to the inferior vena cava using sterile cotton swabs every 10 mL for 15 s to enhance tissue digestion. Excised livers were mechanically dissociated in ice-cold medium (Gibco, A121601) supplemented with 10% FBS and filtered through a 100 mm cell strainer (Biosharp, BS-100-CS). To separate viable cells from non-viable ones, the hepatocyte solution was layered on a 90% Percoll gradient and centrifuged at 200 $\times g$ for 10 min at 4 $^{\circ}\text{C}$. Viable cell pellets were resuspended in plating medium at 80% confluence. Cells were maintained at 37 $^{\circ}\text{C}$ in a humidified 5% CO₂ incubator. Cell viability was confirmed by trypan blue exclusion prior to experimentation.

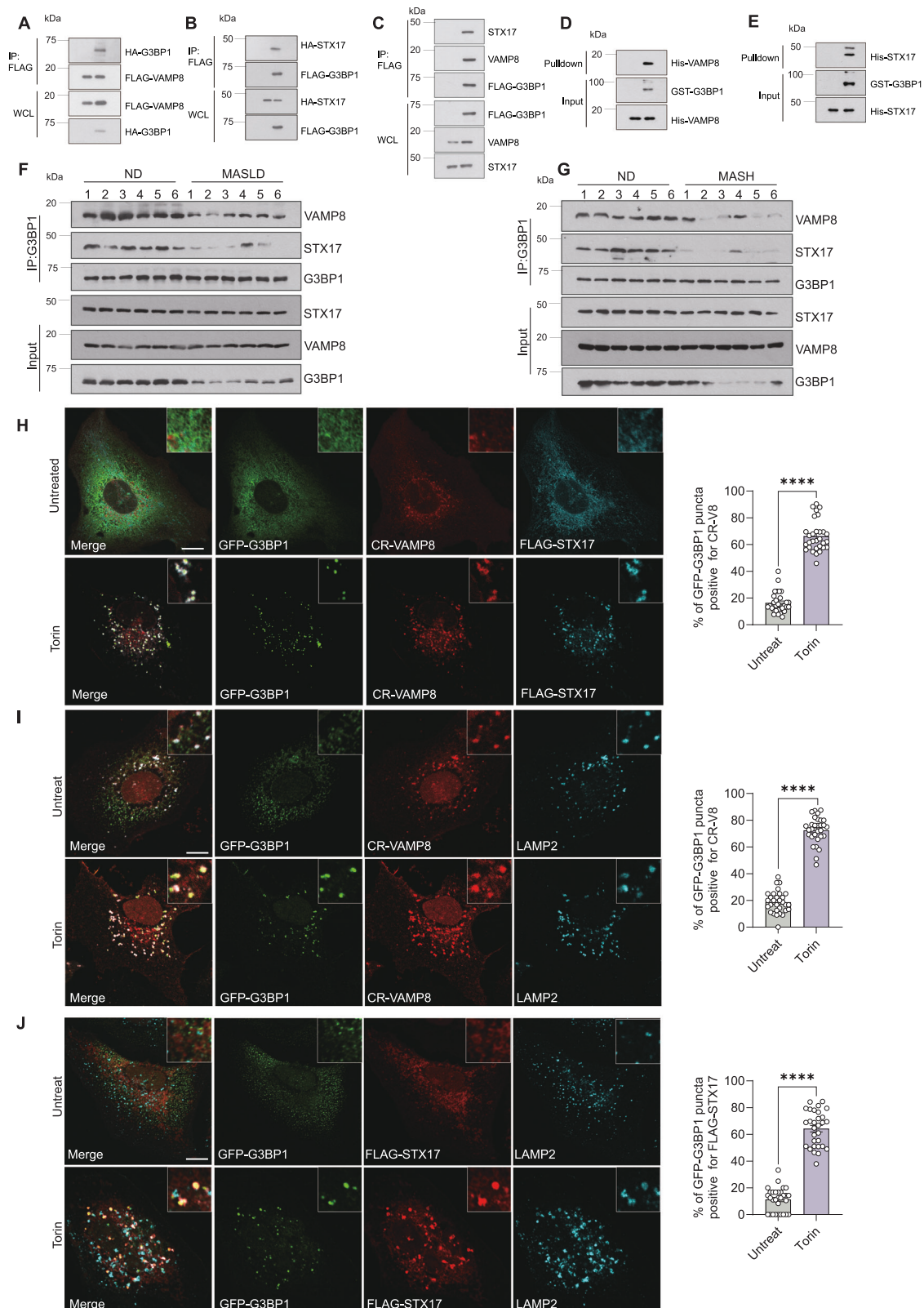
Fractionation assays

Liver tissues from male 8-week-old WT and G3BP1 LKO mice fed HFD for 20 weeks were homogenized in ice-cold lysis buffer (10 mM HEPES pH 7.9, 1.5 mM MgCl₂, 10 mM KCl, 0.5% NP-40, 1 \times protease inhibitor cocktail, Roche 05892791001) using a Dounce homogenizer. The homogenate was centrifuged at 1000 $\times g$ for 10 min (Eppendorf 5430R, 4 $^{\circ}\text{C}$) to pellet nuclei. The supernatant was further centrifuged at 10,000 $\times g$ for 30 min (4 $^{\circ}\text{C}$) to obtain the cytoplasmic fraction. Nuclear pellets were purified through a sucrose density gradient (1.8 M sucrose, 10 mM HEPES pH 7.9, 0.1% Triton X-100) via ultracentrifugation (Beckman Optima XE-90, 100,000 $\times g$, 4 $^{\circ}\text{C}$, 1 h).

Protein concentrations were quantified using the BCA assay (Pierce, 23225). Equal amounts (30 μg) of cytoplasmic or nuclear proteins were resolved on 10% SDS-PAGE gels (Bio-Rad, 4561033) under constant voltage (80 V for 30 min, then 120 V for 1 h). Proteins were transferred to methanol-activated PVDF membranes (Millipore, IPFL00010) using a Trans-Blot Turbo system (Bio-Rad, 1704150) at 80 V for 120 min. Membranes were blocked with 5% non-fat milk for 1 h at room temperature, then incubated overnight at 4 $^{\circ}\text{C}$ with primary antibodies: rabbit anti-TFE3 (Cell Signaling Technology, 14779, 1:1000), mouse anti-14-3-3 (Santa Cruz, sc-1657, 1:2000), or rabbit anti-histone H3 (Abcam, ab1791, 1:5000). After PBST washes (3 \times 10 min), membranes were incubated with HRP-conjugated secondary antibodies (anti-rabbit IgG, Cell Signaling Technology, 7074, 1:5000; anti-mouse IgG, Cell Signaling Technology, 7076, 1:5000) for 1 h at room temperature. Signals were developed with ECL substrate (Beyotime, P0018M) using a ChemiDoc MP imaging system (Bio-Rad) with optimized exposure times (1–300 s).

Co-Immunoprecipitation

Male 8-week-old WT and G3BP1 LKO mice were maintained under specific pathogen-free conditions (22 \pm 2 $^{\circ}\text{C}$, 12-h light/dark cycle) with ad libitum access to either HFD for 20 weeks to establish MASLD or HFHC for 24 weeks to model MASH. To assess protein interactions



between G3BP1 and SNARE complex components in MASLD/MASH pathogenesis, liver tissues from control and disease model mice were homogenized in ice-cold lysis buffer (20 mM Tris-HCl pH 7.4, 150 mM NaCl, 1 mM EDTA, 1% NP-40, 1× protease inhibitor cocktail, Roche, 05892953001) and centrifuged at 12,000 × g for 15 min at 4 °C to collect supernatants. Lysates were pre-cleared with Protein A/G Plus Agarose (Proteintech, PR40025) for 1 h at 4 °C. Equal amounts of lysate

were incubated overnight at 4 °C with anti-G3BP1 antibody (Proteintech, 13057-2-AP) or IgG control (Proteintech, 98136-1-RR) followed by 4 h incubation with Protein A/G magnetic beads. Beads were washed three times with lysis buffer, and bound proteins were eluted by boiling in SDS loading buffer (50 mM Tris-HCl pH 6.8, 2% SDS, 10% glycerol, 4% β-mercaptoethanol, 100 mM DTT, 0.01% bromophenol blue). Eluates were subjected to SDS-PAGE and immunoblotted with

Fig. 5 | G3BP1 functions together with SNARE to promote autophagosome-lysosome fusion. **A** Co-immunoprecipitation (IP) of HA-G3BP1 and FLAG-VAMP8. HEK293T cells were transfected with an empty vector or HA-G3BP1 with Flag-VAMP8. After 24 h of transfection, cell lysates were subjected to immunoprecipitation using an anti-Flag beads. Each experiment was repeated independently at least three times. **B** Co-immunoprecipitation (IP) of HA-STX17 and FLAG-G3BP1. HEK293T cells were transfected with an empty vector or HA-STX17 with Flag-G3BP1. After 24 h of transfection, cell lysates were subjected to immunoprecipitation using an anti-Flag beads. Each experiment was repeated independently at least three times. **C** Co-IP of HEK293T cells transfected with FLAG-G3BP1. HEK293T cells were transfected with empty vector and Flag-G3BP1. 24 h after transfection, cells lysates were immunoprecipitated with anti-Flag beads. VAMP8 and STX17 antibodies were utilized to detect the endogenous proteins. Each experiment was repeated independently at least three times. **D, E** Glutathione Sepharose beads were used to bind GST or GST-G3BP1, which were then incubated with purified His-tagged VAMP8(D) or STX17(E) for 12 h. The eluted samples were subsequently subjected to immunoblotting. Each experiment was repeated independently at least three times. **F** G3BP1-STX17/VAMP8 interaction in murine MASLD livers. Male 8-week-old WT and G3BP1 LKO mice were fed with HFD ad libitum for 20 weeks to induce MASLD ($n = 6$). Control cohorts received normal diet (ND). Co-IP of G3BP1 and STX17/

VAMP8 in hepatic tissues from control and MASLD mice. Lysates from liver homogenates were immunoprecipitated with anti-G3BP1 antibody, followed by immunoblotting for STX17/VAMP8. Each experiment was repeated independently at least three times. **G** G3BP1-VAMP8 interaction in murine MASH livers. Male 8-week-old WT and G3BP1 LKO mice were fed with HFHC ad libitum for 24 weeks to induce MASH ($n = 6$). Control cohorts received normal diet (ND). Co-IP of G3BP1 and STX17/VAMP8 in hepatic tissues. Liver lysates were immunoprecipitated with anti-G3BP1 antibody and immunoblotted for STX17/VAMP8. Each experiment was repeated independently at least three times. **H** HEPG2 cells were transfected with GFP-G3BP1, CR-VAMP8, and FLAG-STX17 in the presence or absence of Torin1 for 2 h followed by confocal immunofluorescence microscopy. Scale bars, 10 μ m. **I** HEPG2 cells were transfected with GFP-G3BP1 and CR-VAMP8 and were stained with an antibody against LAMP2 in the presence or absence of Torin1 for 2 h, followed by confocal immunofluorescence microscopy. Scale bars, 10 μ m. **J** HEPG2 cells were transfected with GFP-G3BP1 and FLAG-STX17 and stained with an antibody against LAMP2 in the presence or absence of Torin1 for 2 h, followed by confocal immunofluorescence microscopy. Scale bars: 10 μ m. In all statistical plots, the data are presented as means \pm S.E.M (at least 30 cells analyzed per group across three independent experiments). For panels (H), (I) and (J), statistical significance was assessed using unpaired two-tailed Student's t -test. **** $P < 0.0001$.

anti-STX17(Sigma-Aldrich, SAB1304559) and anti-VAMP8(Sigma-Aldrich, SAB2107408) antibodies.

For in vitro pulldown assays, recombinant GST and GST-G3BP1 proteins were expressed in *E. coli* BL21(DE3) via 0.5 mM IPTG (Sigma-Aldrich, 16758) induction (16 °C, 18 h), purified using Glutathione Sepharose 4B beads (Cytiva, 17007501) in PBS (pH 7.4, 1% Triton X-100, 1 \times protease inhibitor cocktail, Roche, 05892953001) with three sequential washes (10 CV each), and quantified via Bradford assay (Bio-Rad, 5000006). Purified His-tagged VAMP8 and STX17 (1 mg/mL in 20 mM HEPES pH 7.4, 150 mM NaCl) were incubated with GST/GST-G3BP1-bound beads (10 μ g bait protein/mg beads) in interaction buffer (20 mM Tris-HCl pH 7.5, 350 mM NaCl, 1% Triton-x100, 1 mM EDTA) for 12 h at 4 °C with gentle rotation. Beads were washed 3 times with high-stringency buffer (50 mM Tris-HCl pH 8.0, 500 mM NaCl, 0.5% NP-40), eluted with 10 mM reduced glutathione (Sigma-Aldrich, G4251), and eluates resolved on 12% SDS-PAGE (Bio-Rad, 4561044) for immunoblotting using anti-GST (Proteintech, 10000-0-AP, 1:3000) and anti-His (Sigma-Aldrich, H1029, 1:5000) antibodies.

Liver immunohistochemistry analysis

Paraffin sections were deparaffinized and rehydrated, followed by antigen retrieval using EDTA buffer (pH 9.0, Abcam, ab93684) in a microwave oven (high temperature for 5 min, then low temperature for 15 min). After cooling to room temperature, sections were incubated with 3% H₂O₂ for 15 min to block endogenous peroxidase activity. Blocking was performed with 10% goat serum at room temperature for 1 h, followed by incubation with rabbit anti-G3BP1 antibody (Proteintech, 13057-2-AP) at 4 °C overnight. The sections were then incubated with an immunohistochemical secondary antibody (ZSbio, PA-9001) for 45 min, followed by DAB (3 min, ZSbio, ZLI9018) for color development. Finally, hematoxylin counterstaining was performed, followed by gradient dehydration, clearing with xylene, and mounting with a neutral resinous medium. Whole-slide digital imaging was performed on a Leica Microsystems (DFC450C), with DAB-positive areas quantified in ImageScope 12.4 (Leica) using hue-saturation-intensity thresholds (Hue: 0-30, Saturation: 120-255, Intensity: 90-200).

Knockout of G3BP1 in HEPG2 cells using CRISPR/Cas9

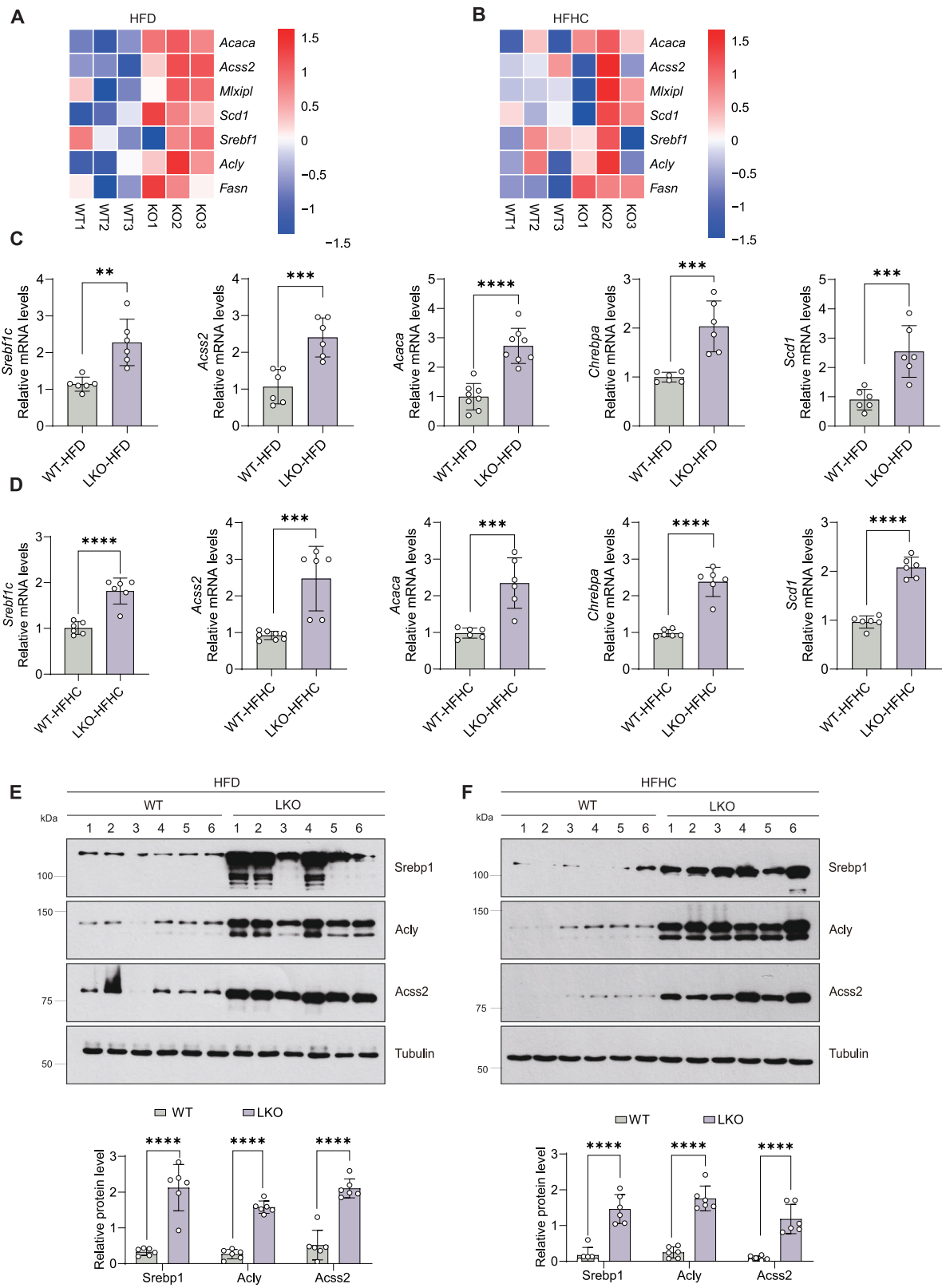
Single-guide RNAs (sgRNAs) targeting exon 3 of human G3BP1 were designed using the MIT CRISPR Design Tool (v2.3.1) with stringent off-target filtering (≤ 2 mismatches in seed regions). Oligonucleotides (Integrated DNA Technologies) were annealed and cloned into the BsmBI-digested LentiV_Cas9_puro vector (Addgene, 108100) via Golden Gate assembly (NEB T4 DNA Ligase, M0202S, 25 °C/16 h).

Lentiviral particles were produced in HEK293T cells (ATCC, CRL-3216) cultured in DMEM (Cytiva, SH30022.01) supplemented with 10% FBS (Thermo Fisher Scientific, A5256701) and 1% P/S (Beyotime, C0222) by co-transfecting 10 μ g transfer plasmid, 3.75 μ g psPAX2 (Addgene, 12260), 1.5 μ g pMD2.G (Addgene, 12259) and 5 μ g LentiV_Cas9_puro_sgG3BP1 using Lipofectamine 3000 (Thermo Fisher Scientific, L3000008). Viral supernatants were collected at 48/72 h post transfection, concentrated via PEG-it (System Biosciences LV825A-1), and titrated by qPCR (Lenti-X RT/RNase Inhibitor Mix Takara, 631280). HEPG2 cells were transduced at MOI 5 with 10 μ g/mL Polybrene (Sigma-Aldrich, TR-1003) for 24 h, followed by puromycin selection (1 μ g/mL, Sigma-Aldrich, P9620) for 72 h. Monoclonal populations were generated by limiting dilution (0.5 cells/well) in 96-well plates. Knockout efficiency was validated by T7E1 assay (NEB, M0302S; 37 °C/30 min) using PCR-amplified genomic DNA (primers: 5'-GCTGGTGTGGAGAGTGAGG-3', 3'-CAGGGTCTCCTTGAGCTTCC-3'). Functional knockout was confirmed by immunoblotting (anti-G3BP1, Proteintech, 13057-2-AP, 1:1000) showing >90% protein reduction compared to scramble sgRNA controls.

RNA sequencing

Liver tissues from male 8-week-old WT and G3BP1 LKO mice were analyzed following induction of MASLD or MASH via dietary interventions: MASLD was modeled by feeding HFD for 20 weeks, while MASH was induced using HFHC for 24 weeks. Total RNA was isolated from mouse liver tissues using TRIzol Reagent (Invitrogen, 15596026) with mechanical homogenization (Precellys Evolution Homogenizer, Bertin Technologies, 5 \times 30 s pulses at 6500 rpm) followed by chloroform phase separation (12,000 \times g, 15 min, 4 °C). RNA integrity was verified using an Agilent 4200 TapeStation (RNA Integrity Number [RIN] ≥ 8.0 , DV200 > 80%) and quantified by UV-Vis spectroscopy (NanoDrop One, Thermo Fisher Scientific). Poly(A)-enriched libraries were prepared with the NEBNext Ultra II RNA Library Prep Kit (NEB, E7770S) using 1 μ g input RNA, including RNA fragmentation (94 °C for 8 min), first-strand cDNA synthesis with random hexamers (ProtoScript II Reverse Transcriptase), and dual-size selection via AMPure XP Beads (Beckman Coulter, A63881; 0.6 \times and 1.2 \times ratios) to retain 150–200 bp inserts. Libraries were quantified by Qubit 4.0 (Thermo Fisher Scientific, Q33238) and validated for size distribution (Agilent High Sensitivity DNA Kit, 5067-4626) before sequencing on an Illumina NovaSeq 6000 platform (Illumina, 20012850) with paired-end 150 bp reads (40 million reads/sample, Q30 $\geq 85\%$).

Raw reads underwent quality control with FastQC (v0.11.9) and adapter trimming by Trimmomatic (v0.39, SLIDINGWINDOW:4:20).



HISAT2 aligned reads to the GRCm38 reference genome (ENSEMBL release 102). Mapped reads were counted via HTSeq with GENCODE M25 annotations.

Quantitative real-time PCR analysis

Total RNA was isolated from 50 mg liver tissue using TRIzol Reagent (Invitrogen, 15596026) with mechanical homogenization (Precellys

Evolution, 3 × 30 s pulses at 6500 rpm), followed by chloroform phase separation (12,000 × g, 15 min, 4 °C) and isopropanol precipitation. RNA integrity was verified (RIN ≥ 8.0, Agilent 2100 Bioanalyzer) prior to reverse transcription using the HiScript III 1st Strand cDNA Synthesis Kit (Vazyme, R312-01) with oligo(dT)20 primers under recommended conditions (50 °C for 30 min, 85 °C for 5 min, Eppendorf Mastercycler Nexus). cDNA was diluted 1:20 in nuclease-free water (Thermo Fisher

Fig. 6 | Hepatic knockout of G3BP1 KO exacerbates HFD-induced MASLD and HFHC-induced MASH in mice by promoting a de novo lipogenesis transcriptional program. Male 8-week-old WT and G3BP1 LKO mice fed HFD for 20 weeks (MASLD model, **A**) or HFHC for 24 weeks (MASH model, **B**). Liver mRNA were extracted and subjected to RNA-seq analysis ($n = 3$). Heatmap of RNA-seq data showing Z-score-normalized expression of de novo lipogenesis-related genes (*Srebp1c*, *Acs2*, *Acaca*, *Chrebp*, and *Scd1*). **C**, **D** qPCR of de novo lipogenesis genes of *Srebp1c*, *Acs2*, *Acaca*, *Chrebp*, and *Scd1* in liver tissues from the same experimental

Scientific, AM9937) and amplified using SYBR qPCR Master Mix(U+) (Vazyme, Q713-02) on a QuantStudio 5 Real-Time PCR System (Applied Biosystems) with the following cycling parameters: 95 °C for 30 s; 40 cycles of 95 °C for 10 s, 60 °C for 30 s, and 72 °C for 20 s. Gene-specific primers were validated for specificity (single-peak melt curves) and efficiency (90–105%). Data were normalized to β -actin ($\Delta\Delta C_t$ method) using primers: Forward 5'-CATGTACGTTGCTATCCAGGC-3', Reverse 5'-CTCCTTAATGTCACGCACGAT-3', with inter-run CV < 5% and no-template controls confirming absence of genomic DNA contamination. Statistical significance was determined by Student's *t*-test (GraphPad Prism 9.4.1, $P < 0.05$).

Human-*IL-6* forward: ACTCACCTCTTCAGAACGAATTG
 Human-*IL-6* reverse: CCATCTTTGGAAGGTTTCAGGTTG
 Human-TNF α forward: CCTCTCTCTAATCAGCCCTCTG
 Human-TNF α reverse: GAGGACCTGGGAGTAGATGAG Mouse-
 Acta2 forward: ATGCTCCCAGGGCTGTTTCCCCTAT
 Mouse-Acta2 reverse: GTGGTGCCAGATCTTTTCCATGTCCG
 Mouse-*Col1a1* forward: GCTCCTCTTAGGGGCCACT
 Mouse-*Col1a1* reverse: CCACGTCTCACCATTGGGG
 Mouse-*Tgfb1* forward: CTCCCGTGGCTTCTAGTGC
 Mouse-*Tgfb1* reverse: GCCTTAGTTTGGACAGGATCTG
 Mouse-*Timp1* forward: ATATCCGGTACGCCTACACC
 Mouse-*Timp1* reverse: GCCCGTGATGAGAACTCTT
 Mouse-Tnf α forward: GACGTGGAAGTGGCAGAAGAG
 Mouse-Tnf α reverse: TTGGTGGTTTGTGAGTGTGAG
 Mouse-*Il6* forward: TAGTCCTTCTACCCCAATTTC
 Mouse-*Il6* reverse: TTGGTCCTTAGCCACTCCTTC

TC and TG analysis

Total cholesterol levels were quantified using T-CHO assay kit (Nanjing Jiancheng Bioengineering Institute, A111-1-1) and Triglycerides were quantified using Triglyceride assay kit (Nanjing Jiancheng Bioengineering Institute, A110-1-1). Liver tissues (10 mg) from euthanized mice were homogenized in 200 μ L ice-cold absolute ethanol using a Precellys 24 homogenizer (3 \times 20 s pulses at 6500 rpm, Bertin Technologies). Lysates were clarified by centrifugation (12,000 $\times g$, 15 min, 4 °C) to collect the lipid-rich supernatant. The enzymatic reaction was initiated by mixing 2.5 μ L of liver homogenate or serum with 250 μ L of working reagent (50 mmol/L Good's buffer, pH 6.7, containing cholesterol esterase ≥ 50 KU/L, cholesterol oxidase ≥ 25 KU/L, peroxidase ≥ 1.3 KU/L, and 0.3 mmol/L 4-AAP) in 96-well plates. After 10 min incubation at 37 °C, absorbance was measured at 500 nm. Triglycerides (TG) was performed by mixing 2.5 μ L of liver homogenate or serum with 250 μ L of working reagent (100 mmol/L Tris-HCl buffer, pH 7.4, containing lipase ≥ 3000 U/L, glycerol kinase ≥ 1000 U/L, glycerol-3-phosphate oxidase ≥ 5000 U/L, peroxidase ≥ 1000 U/L, 1.4 mmol/L 4-aminoantipyrine, and 3 mmol/L 4-chlorophenol) in 96-well plates. After 10 min incubation at 37 °C, absorbance was measured at 500 nm.

Mouse liver function assays

For glucose tolerance tests (GTT), mice ($n = 8$ /group) were fasted 16 h with ad libitum access to water in clean cages. A 20% (*w/v*) D-glucose solution (Sigma, G8270) was dissolved in saline and prewarmed to 37 °C. Mice received an intraperitoneal (IP) injection of the glucose solution at a volume of 10 mL per kg body weight, delivering a dose of 2 g glucose/kg. For Insulin tolerance tests (ITT), mice ($n = 8$ /group)

were fasted 4 h with ad libitum access to water in clean cages. Human recombinant insulin (Thermo Fisher Scientific, 12585014) was reconstituted in saline to a final concentration of 0.075 IU/mL. Mice received an IP injection of the insulin solution at a volume of 10 mL per kg body weight, resulting in a dose of 0.75 IU insulin/kg. Blood glucose was monitored at 0/15/30/60/90/120 min post injection via tail nick sampling using a Contour Next One glucometer (Ascensia Diabetes Care, 5 μ L blood/sample, technical duplicates).

For serum biochemistry, blood samples were collected from the retro-orbital venous plexus using heparinized capillary tubes under brief isoflurane anesthesia and transferred into serum separation tubes (BD, 365967). Tubes were allowed to clot at room temperature for 30 min, followed by centrifugation at 3000 $\times g$ for 15 min at 4 °C (Eppendorf 5430 R) to isolate serum. Alanine aminotransferase (ALT) and aspartate aminotransferase (AST) activities were measured using commercial kits (Nanjing Jiancheng Bioengineering, C009-2-1 for ALT and C010-2-1 for AST) on an ELISA reader (Siemens 11086322) with photometric detection at 505 nm (37 °C).

For serum biochemistry, blood samples were collected from the retro-orbital venous plexus using heparinized capillary tubes under brief isoflurane anesthesia and transferred into serum separation tubes (BD, 365967). Tubes were allowed to clot at room temperature for 30 min, followed by centrifugation at 3000 $\times g$ for 15 min at 4 °C (Eppendorf 5430 R) to isolate serum. Alanine aminotransferase (ALT) and aspartate aminotransferase (AST) activities were measured using commercial kits (Nanjing Jiancheng Bioengineering, C009-2-1 for ALT and C010-2-1 for AST) on an ELISA reader (Siemens 11086322) with photometric detection at 505 nm (37 °C).

Immunoblotting

Liver tissues (human/mouse) were homogenized in ice-cold RIPA lysis buffer (Beyotime, P0013B, supplemented with 1 \times protease/phosphatase inhibitor cocktail, Roche 05892791001) using a Precellys 24 homogenizer (3 \times 30 s pulses at 6500 rpm), while primary hepatocytes and HepG2 cells were lysed in SDS buffer (50 mM Tris-HCl pH 6.8, 2% SDS, 10% glycerol, 4% β -mercaptoethanol, 100 mM DTT, 0.01% bromophenol blue) with brief sonication (Qsonica Q700, 20% amplitude, 3 \times 5 s pulses). Lysates were clarified by centrifugation (14,000 $\times g$, 15 min, 4 °C), quantified via BCA assay (Pierce, 23225), and 30 μ g protein/sample resolved on 15% SDS-PAGE gels (Bio-Rad 4561036) under constant voltage (80 V for 30 min, 120 V for 1 h). Proteins were transferred to methanol-activated PVDF membranes (Millipore, IPFL00010) using a Trans-Blot Turbo system (Bio-Rad, 1704150) at 80 V for 120 min. Membranes were blocked with 5% non-fat milk (BD, 232100) in PBST 137 mmol/L (NaCl, 2.7 mmol/L KCl, 4.3 mmol/L Na₂HPO₄, 1.4 mmol/L KH₂PO₄, 0.1% Tween-20, pH 7.2–7.4) for 1 h at RT, followed by overnight incubation at 4 °C with primary antibodies: rabbit anti-G3BP1 (Proteintech, 13057-2-AP, 1:1000), mouse anti-LC3B (Sigma-Aldrich, L7543, 1:2000), rabbit anti-LAMP2 (Santa Cruz, sc-18822, 1:500), mouse anti-FLAG (Sigma-Aldrich, F7425, 1:5000), and mouse anti- β -tubulin (Sigma-Aldrich, T8328, 1:10,000). After 3 \times 10 min PBST washes, membranes were incubated with HRP-conjugated secondary antibodies (Proteintech, SA00001-1 anti-mouse, 1:5000; SA00001-2 anti-rabbit, 1:5000) for 1 h at RT. Signals were developed with ECL Plus (Beyotime, P0018M) using a ChemiDoc MP imaging system (Bio-Rad) with optimized exposure times (1–300 s), and band intensities quantified via Image Lab 6.1 software normalized to β -tubulin.

Transmission electron microscopy of liver tissue

Liver specimens were rapidly harvested from euthanized C57BL/6J mice ($n = 6$ /group) and immediately dissected into 0.5 mm³ cubes within 2 min post mortem to minimize autolytic changes. Tissue fragments were immersion-fixed in 2.5% glutaraldehyde (Solarbio, PI126) in 0.1 M sodium cacodylate buffer (pH 7.4, 320 mOsm/kg H₂O) supplemented with 2 mM CaCl₂ for 24 h at 4 °C, followed by three

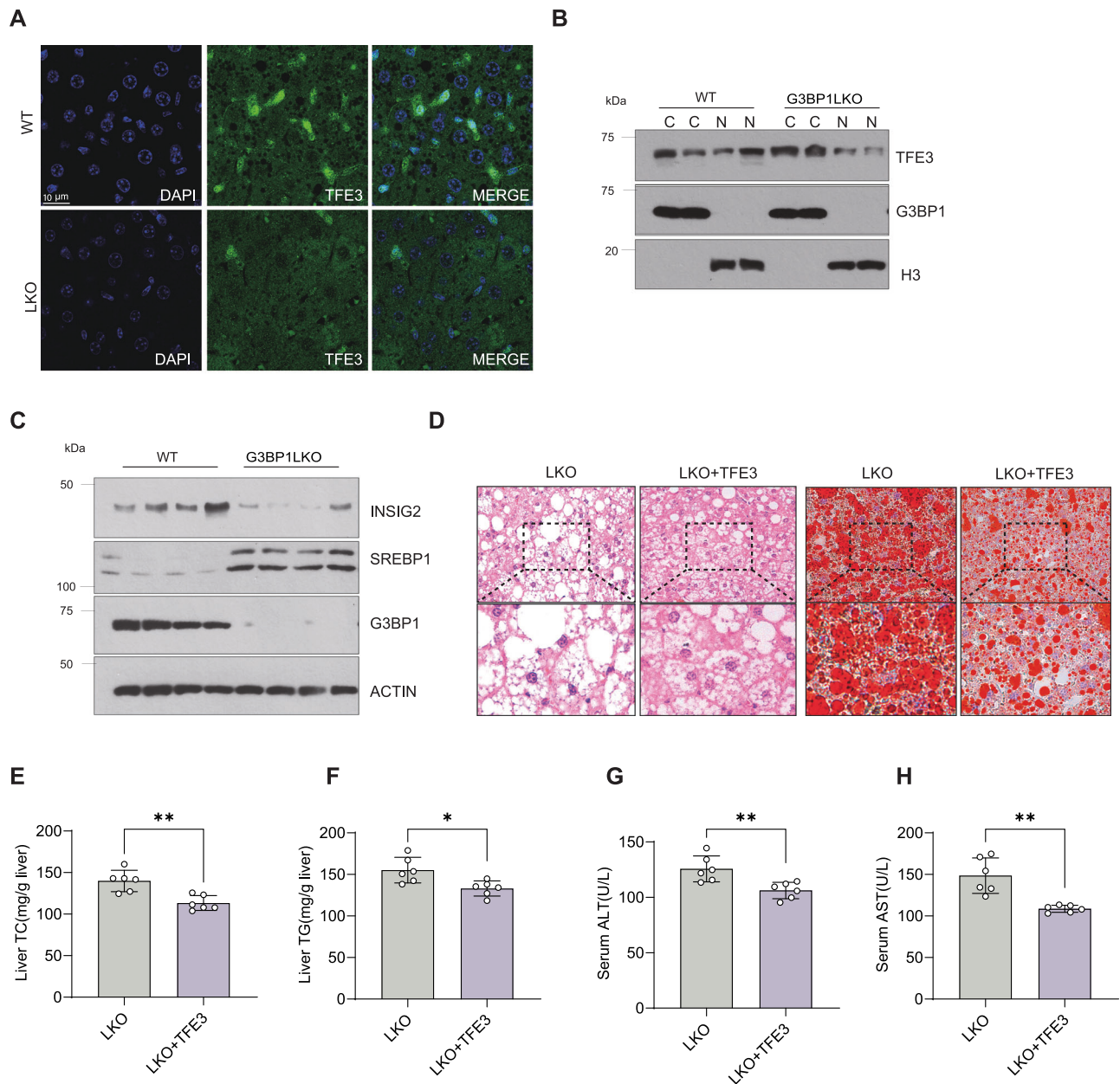


Fig. 7 | G3BP1 is required for de novo lipogenesis. **A** Male 8-week-old WT and G3BP1 LKO mice fed HFD for 20 weeks (MASLD model, $n = 6$ mice per group). Liver cryosections were fixed in 4% paraformaldehyde and subjected to immunofluorescence staining using TFE3 antibody. Nuclei were counterstained with DAPI. Scale bar: 10 μm . **B** Cytoplasmic and nuclear fractions were isolated from livers of male 8-week-old WT and G3BP1 LKO mice fed HFD for 20 weeks. Fraction purity was validated by immunoblotting with anti-Histone H3 for nuclear markers. Parallel blots were probed with anti-TFE3, anti-Tubulin, and anti-G3BP1. Each experiment was repeated independently at least three times. **C** Liver lysates from male 8-week-old WT and G3BP1 LKO mice fed HFD for 20 weeks were resolved by SDS-PAGE for Western blot analysis ($n = 4$). Membranes were probed with anti-INSIG2, anti-SREBP1 and anti-G3BP1. ACTIN served as loading control. **D** 8-week-old G3BP1 LKO

male mice were intravenously injected with AAV8-Control or AAV8-TFE3 (2×10^{11} viral genomes/mouse) and maintained on HFD for 20 weeks. Representative liver sections stained with H&E (left panels) and Oil Red O (right panels) are shown. Scale bars: 50 μm . $n = 6$ biologically independent mice per group. Hepatic triglyceride (TG, **E**) and total cholesterol (TC, **F**) levels in AAV8-treated G3BP1 LKO mice ($n = 6$ mice per group). All values are presented as means \pm S.E.M. Statistical significance was assessed using unpaired two-tailed Student's t -test. Exact P value for TG (Panel **E**), $*P = 0.012$; TC (Panel **F**), $**P = 0.0042$. Serum ALT (**G**) and AST (**H**) activities in the indicated groups ($n = 6$ mice per group). All values are presented as means \pm S.E.M. Statistical significance was assessed using unpaired two-tailed Student's t -test. Exact P value for ALT (panel **G**), $**P = 0.0062$; for AST (panel **H**), $**P = 0.0012$.

10 min washes in cacodylate buffer containing 50 mM glycine to quench residual aldehydes. Post-fixation was performed in 1% osmium tetroxide/1.5% potassium sferrocyanide in 0.1 M cacodylate buffer (pH 6.8) for 2 h at 4 $^{\circ}\text{C}$ to enhance membrane contrast, with subsequent en bloc staining in 2% aqueous uranyl acetate overnight at 4 $^{\circ}\text{C}$. Dehydration through a graded ethanol series (30% to 100%) incorporated a progressive temperature decrease (4 $^{\circ}\text{C}$ to 20 $^{\circ}\text{C}$) during high-concentration ethanol steps to preserve lipid content. Tissue

infiltration used Spurr's epoxy resin via a 3:1 acetone-resin mixture (4 h), 1:1 transition (8 h), and pure resin (24 h under vacuum), followed by polymerization at 60 $^{\circ}\text{C}$ for 48 h under nitrogen. Ultrathin sections (70 nm) cut with a diatome diamond knife on a Leica UC7 ultramicrotome were collected on formvar-coated nickel grids and dual-stained with Reynolds' lead citrate (5 min) and 2% uranyl acetate (10 min) in an argon chamber. Imaging on a JEOL JEM-1400Flash TEM at 120 kV captured multi-scale micrographs (2500 \times –50,000 \times),

Number of autophagosome were counted and normalized to the total area of the cell.

Statistical analysis

All values are presented as means \pm S.E.M. 2-tailed *t* tests were used to analyze differences between two groups. For comparisons among multiple groups, two-way ANOVA was employed. **P* < 0.05; ***P* < 0.01; ****P* < 0.001; *****P* < 0.0001 and the statistical methods used along with the corresponding *P* values are indicated in each figure caption.

Reporting summary

Further information on research design is available in the Nature Portfolio Reporting Summary linked to this article.

Data availability

Published datasets used in this study are available in the NCBI Gene Expression Omnibus, under accessions GSE162694 and GSE126848. The RNA-seq are available under accession code GSE304454 (<https://www.ncbi.nlm.nih.gov/geo/query/acc.cgi?acc=GSE304454>). Source data are provided with this paper. All data supporting the findings of this study are available within the paper and its Supplementary Information. Source data are provided with this paper.

References

- Rinella, M. E. et al. A multisociety Delphi consensus statement on new fatty liver disease nomenclature. *Ann. Hepatol.* **29**, 101133 (2024).
- Friedman, S. L. et al. Mechanisms of NAFLD development and therapeutic strategies. *Nat. Med.* **24**, 908–922 (2018).
- Loomba, R. & Sanyal, A. J. The global NAFLD epidemic. *Nat. Rev. Gastroenterol. Hepatol.* **10**, 686–690 (2013).
- Anstee, Q. M., Targher, G. & Day, C. P. Progression of NAFLD to diabetes mellitus, cardiovascular disease or cirrhosis. *Nat. Rev. Gastroenterol. Hepatol.* **10**, 330–344 (2013).
- Byrne, C. D. & Targher, G. NAFLD: a multisystem disease. *J. Hepatol.* **62**, S47–S64 (2015).
- Anstee, Q. M. et al. From NASH to HCC: current concepts and future challenges. *Nat. Rev. Gastroenterol. Hepatol.* **16**, 411–428 (2019).
- Michelotti, G. A., Machado, M. V. & Diehl, A. M. NAFLD, NASH and liver cancer. *Nat. Rev. Gastroenterol. Hepatol.* **10**, 656–665 (2013).
- Ratzliff, V., Goodman, Z. & Sanyal, A. Current efforts and trends in the treatment of NASH. *J. Hepatol.* **62**, S65–S75 (2015).
- Musso, G., Cassader, M. & Gambino, R. Non-alcoholic steatohepatitis: emerging molecular targets and therapeutic strategies. *Nat. Rev. Drug Discov.* **15**, 249–274 (2016).
- Prentzell et al. G3BPs tether the TSC complex to lysosomes and suppress mTORC1 signaling. *Cell* **184**, 655–674 e27 (2021).
- Alam, U. & Kennedy, D. Rasputin a decade on and more promiscuous than ever? A review of G3BPs. *Biochim. Biophys. Acta Mol. Cell Res.* **1866**, 360–370 (2019).
- Costa, M. et al. Human DNA helicase VIII: a DNA and RNA helicase corresponding to the G3BP protein, an element of the ras transduction pathway. *Nucleic Acids Res.* **27**, 817–821 (1999).
- Sanders, D. W. et al. Competing protein-RNA Interaction Networks Control Multiphase Intracellular Organization. *Cell* **181**, 306–324 e28 (2020).
- Guillen-Boixet, J. et al. RNA-induced conformational switching and clustering of G3BP drive stress granule assembly by condensation. *Cell* **181**, 346–361 e17 (2020).
- Liu, Z. S. et al. G3BP1 promotes DNA binding and activation of cGAS. *Nat. Immunol.* **20**, 18–28 (2019).
- Yamamoto, H., Zhang, S. & Mizushima, N. Autophagy genes in biology and disease. *Nat. Rev. Genet.* **24**, 382–400 (2023).
- Morishita, H. & Mizushima, N. Diverse cellular roles of autophagy. *Annu. Rev. Cell Dev. Biol.* **35**, 453–475 (2019).
- Zhao, Y. G., Codogno, P. & Zhang, H. Machinery, regulation and pathophysiological implications of autophagosome maturation. *Nat. Rev. Mol. Cell Biol.* **22**, 733–750 (2021).
- Qian, H. et al. Autophagy in liver diseases: a review. *Mol. Asp. Med.* **82**, 100973 (2021).
- Zhao, Y. G. & Zhang, H. Autophagosome maturation: an epic journey from the ER to lysosomes. *J. Cell Biol.* **218**, 757–770 (2019).
- Soreng, K., Neufeld, T. P. & Simonsen, A. Membrane trafficking in autophagy. *Int. Rev. Cell Mol. Biol.* **336**, 1–92 (2018).
- Galluzzi, L. et al. Molecular definitions of autophagy and related processes. *EMBO J.* **36**, 1811–1836 (2017).
- Itakura, E., Kishi-Itakura, C. & Mizushima, N. The hairpin-type tail-anchored SNARE syntaxin 17 targets to autophagosomes for fusion with endosomes/lysosomes. *Cell* **151**, 1256–1269 (2012).
- Singh, R. et al. Autophagy regulates lipid metabolism. *Nature* **458**, 1131–1135 (2009).
- Czaja, M. J. et al. Functions of autophagy in normal and diseased liver. *Autophagy* **9**, 1131–1158 (2013).
- Lan, T. et al. Hepatocyte glutathione S-transferase mu 2 prevents non-alcoholic steatohepatitis by suppressing ASK1 signaling. *J. Hepatol.* **76**, 407–419 (2022).
- Schuster, S. et al. Triggering and resolution of inflammation in NASH. *Nat. Rev. Gastroenterol. Hepatol.* **15**, 349–364 (2018).
- Zubiete-Franco, I. et al. Methionine and S-adenosylmethionine levels are critical regulators of PP2A activity modulating lipophagy during steatosis. *J. Hepatol.* **64**, 409–418 (2016).
- Klionsky, D. J. et al. Guidelines for the use and interpretation of assays for monitoring autophagy in higher eukaryotes. *Autophagy* **4**, 151–175 (2008).
- Klionsky, D. J. et al. Guidelines for the use and interpretation of assays for monitoring autophagy (4th edition). *Autophagy* **17**, 1–382 (2021).
- Takats, S. et al. Autophagosomal Syntaxin17-dependent lysosomal degradation maintains neuronal function in *Drosophila*. *J. Cell Biol.* **201**, 531–539 (2013).
- Mews, P. et al. Acetyl-CoA synthetase regulates histone acetylation and hippocampal memory. *Nature* **546**, 381–386 (2017).
- Ishii, S. et al. Carbohydrate response element binding protein directly promotes lipogenic enzyme gene transcription. *Proc. Natl Acad. Sci. USA* **101**, 15597–15602 (2004).
- Chajes, V. et al. Acetyl-CoA carboxylase alpha is essential to breast cancer cell survival. *Cancer Res.* **66**, 5287–5294 (2006).
- Foretz, M. et al. Sterol regulatory element binding protein-1c is a major mediator of insulin action on the hepatic expression of glucokinase and lipogenesis-related genes. *Proc. Natl Acad. Sci. USA* **96**, 12737–12742 (1999).
- Ntambi, J. M. & Miyazaki, M. Recent insights into stearyl-CoA desaturase-1. *Curr. Opin. Lipidol.* **14**, 255–261 (2003).
- Gosis, B. S. et al. Inhibition of nonalcoholic fatty liver disease in mice by selective inhibition of mTORC1. *Science* **376**, 264 (2022).
- Fujimoto, Y. et al. TFE3 controls lipid metabolism in adipose tissue of male mice by suppressing lipolysis and thermogenesis. *Endocrinology* **154**, 3577–3588 (2013).
- Kim, D. H. et al. mTOR interacts with raptor to form a nutrient-sensitive complex that signals to the cell growth machinery. *Cell* **110**, 163–175 (2002).
- Martina, J. A. et al. The nutrient-responsive transcription factor TFE3 promotes autophagy, lysosomal biogenesis, and clearance of cellular debris. *Sci. Signal.* **7**, ra9 (2014).
- Yang, P. et al. G3BP1 is a tunable switch that triggers phase separation to assemble stress granules. *Cell* **181**, 325–345 e28 (2020).
- Gwon, Y. et al. Ubiquitination of G3BP1 mediates stress granule disassembly in a context-specific manner. *Science* **372**, eabf6548 (2021).

43. Markmiller, S. et al. Context-dependent and disease-specific diversity in protein interactions within stress granules. *Cell* **172**, 590–604 e13 (2018).
44. Hu, S. et al. PKR-dependent cytosolic cGAS foci are necessary for intracellular DNA sensing. *Sci. Signal.* **12**, 1–13 (2019).
45. Kang, W. et al. Research progress on the structure and function of G3BP. *Front. Immunol.* **12**, 718548 (2021).
46. Martina, J. A. et al. TFEB and TFEB3 are novel components of the integrated stress response. *EMBO J.* **35**, 479–495 (2016).
47. Attia, S. L., Softic, S. & Mouzaki, M. Evolving role for pharmacotherapy in NAFLD/NASH. *Clin. Transl. Sci.* **14**, 11–19 (2021).
48. Wong, V. W. et al. Noninvasive biomarkers in NAFLD and NASH - current progress and future promise. *Nat. Rev. Gastroenterol. Hepatol.* **15**, 461–478 (2018).
49. Brunt, E. M. et al. Nonalcoholic fatty liver disease (NAFLD) activity score and the histopathologic diagnosis in NAFLD: distinct clinicopathologic meanings. *Hepatology* **53**, 810–820 (2011).
50. Kim, D. et al. Graph-based genome alignment and genotyping with HISAT2 and HISAT-genotype. *Nat. Biotechnol.* **37**, 907–915 (2019).
51. Robinson, M. D., McCarthy, D. J. & Smyth, G. K. edgeR: a Bioconductor package for differential expression analysis of digital gene expression data. *Bioinformatics* **26**, 139–140 (2010).
52. Love, M. I., Huber, W. & Anders, S. Moderated estimation of fold change and dispersion for RNA-seq data with DESeq2. *Genome Biol.* **15**, 550 (2014).
53. Chantranupong, L. et al. The CASTOR proteins are arginine sensors for the mTORC1 pathway. *Cell* **165**, 153–164 (2016).
54. Song, Q. et al. Bifidobacterium pseudolongum-generated acetate suppresses non-alcoholic fatty liver disease-associated hepatocellular carcinoma. *J. Hepatol.* **79**, 1352–1365 (2023).
55. Chen, B. et al. Gut bacteria alleviate smoking-related NASH by degrading gut nicotine. *Nature* **610**, 562–568 (2022).

Acknowledgements

This research was funded by National Natural Science Foundation of China (32361163613 92354302-1, 3240801), National Key Research and Development Program of China(2024YFF1106001) to R.L.

Author contributions

Qinqin Ouyang, Jiaqi Su and Yixuan Li performed most of the wet-lab experiments; Haiping Liao performed data analysis; Haiying Guo, Yanan Sun, Xiaoyu Wang and Juan Chen assisted in performing in vivo and

in vitro studies. Josephine Thinwa, Wen-Xing Ding and Herbert Tilg provided critical insights. Fazheng Ren, Hao Zhang and Rong Liu supervised the project.

Competing interests

The authors declare no competing interests.

Additional information

Supplementary information The online version contains supplementary material available at <https://doi.org/10.1038/s41467-025-63022-z>.

Correspondence and requests for materials should be addressed to Fazheng Ren, Hao Zhang or Rong Liu.

Peer review information *Nature Communications* thanks Tushar Patel and the other, anonymous, reviewer(s) for their contribution to the peer review of this work. A peer review file is available.

Reprints and permissions information is available at <http://www.nature.com/reprints>

Publisher's note Springer Nature remains neutral with regard to jurisdictional claims in published maps and institutional affiliations.

Open Access This article is licensed under a Creative Commons Attribution-NonCommercial-NoDerivatives 4.0 International License, which permits any non-commercial use, sharing, distribution and reproduction in any medium or format, as long as you give appropriate credit to the original author(s) and the source, provide a link to the Creative Commons licence, and indicate if you modified the licensed material. You do not have permission under this licence to share adapted material derived from this article or parts of it. The images or other third party material in this article are included in the article's Creative Commons licence, unless indicated otherwise in a credit line to the material. If material is not included in the article's Creative Commons licence and your intended use is not permitted by statutory regulation or exceeds the permitted use, you will need to obtain permission directly from the copyright holder. To view a copy of this licence, visit <http://creativecommons.org/licenses/by-nc-nd/4.0/>.

© The Author(s) 2025